

Controlling the resonant frequency and maximising kinetic inductance of NbN/NbTiN on chip coplanar waveguide resonator for qubit control and readout

*M.Sc. Project stage II (PH595) Report submitted in partial fulfillment for
the award of degree of*

Master of Science

in

Physics

by

**Aakash Shandilya
215120031**

Under the supervision of

Dr. Suddhasatta Mahapatra



DEPARTMENT OF PHYSICS

INDIAN INSTITUTE OF TECHNOLOGY BOMBAY

Acknowledgement

I would like to express my profound gratitude to my guide Prof. Suddhasatta Mahapatra for his kind help in my work. I am deeply indebted to him for his valuable guidance, suggestions and constant encouragement throughout my project work. Furthermore, I would like to thank Siddarth Rastogi, Varsha Jangir, Sounak Samanta, Bikas, Sana Ayyub, Pinki and Dhamma for their help and creative inputs, this work would not have taken its present form without them. The work reported in this thesis was carried out at the Center of Excellence in Nanoelectronics (CEN) Department of Electrical Engineering at IIT Bombay. I would also like to thank all people directly or indirectly involved in my project.

Abstract

When two qubits are separated by a long distance, entangling them becomes impossible as their wavefunctions have zero overlap. To make them interact they are coupled to a resonator. Superconducting qubits have been coupled using this method for a long time, to implement two qubit gates. The intent of this project is to design a resonator to entangle two physically separated spin qubits as well as develop a fabrication process for them.

Contents

Acknowledgement	i
Abstract	ii
1 Introduction	1
1.1 Spin qubits and long-distance qubit coupling	1
1.2 Spin photon coupling	3
1.3 Fundamentals of Microwave Resonators	4
1.3.1 Theory for Transmission lines	4
1.3.2 Terminated Lossless Transmission line	7
1.3.3 Transmission line resonators	9
2 Background work	13
3 Methodology and Processes	17
3.1 Sputtering	17
3.2 Electron Beam Lithography	19
3.3 Reactive Ion Etching	21
4 Troubleshooting	23
4.1 Fabrication process	23
4.2 Lithography	23
4.3 Design file/GDS file	30
4.4 Etching and Sputtering	33
4.5 Final recipes	35
5 Results	37
5.1 Simulation	37
5.2 Sputtering	41
5.3 Fabrication	44
5.4 Resonator measurement	44
Future Work	46

List of Figures

1.1	(a) Cross-section of Si/SiGe heterostructures that confine electrons in the vertical direction. Left: Schematic of the heterostructure. Right: TEM of a heterostructure. (b) False coloured SEM of a double quantum dot(DQD)	2
1.2	Schematic of a typical coplanar waveguide to couple superconducting qubits	4
1.3	(a) Transmission line representation and its voltage and current (b) Equivalent lumped element circuit	5
1.4	Transmission line terminated with load impedance Z_L	7
1.5	Transmission line terminated with open circuit	8
1.6	A parallel RLC circuit	9
1.7	An open circuited lossy transmission line and its voltage distributions for $n = 1$ and $n = 2$	10
1.8	Coplanar waveguide dimensions	12
2.1	NbN film characterization for different sputtering temperatures [1]	13
2.2	Characteristic impedance of resonators with different designs [1]	14
2.3	SEM images of the three resonators [1]	14
2.4	Internal quality factor, Q_i vs the average photon number inside the resonator, $\langle n_{ph} \rangle$ for the three resonators [1]	14
2.5	Optical image of the resonator and the two double quantum dots at its ends [2]	15
2.6	Square of the ratio of the transmitted amplitude to the incident amplitude of the microwave vs frequency of the microwave [2]	15
2.7	(A) SEM image of the centre conductor of the resonator, (B) Optical micrograph of the resonator, (C) SEM of the double quantum dot [3] . . .	16
3.1	Sputter deposition	18
3.2	Comparison of various aspects of Electron Beam Lithography(EBL) and Photolithography	19
3.3	Microscope column of an EBL	20
3.4	The inelastic and elastic scattering of the electron beam on interaction with resist	21
3.5	Diagram showing Reactive Ion Etching process	22

4.1	Overview of all the fabrication processes required to make the resonator . .	23
4.2	Stitching error	24
4.3	Improper exposure	25
4.4	Round edges and thick central strip	25
4.5	The pad with tapered edges connecting to the central strip	27
4.6	Resist residue	27
4.7	Kink at the junction	28
4.8	Broken central strip	28
4.9	Central strip	29
4.10	Junction	29
4.11	Meander	29
4.12	Coupling Capacitor	30
4.13	Pad	30
4.14	Resonator design	30
4.15	FBMS paths with 200 nm of overlap and and gap of 600 nm left in the middle	31
4.16	Transition from wider region into the resonator	31
4.17	Meander	32
4.18	Capacitor	32
4.19	Pad	33
4.20	Rough edges	33
4.21	Unetched NbN creating a short	34
4.22	Some images of the issues that we were facing with NbN etching	34
4.23	Perfect etching but the films were deposited after doing clean biasing . . .	35
5.1	Resonator simulated on HFSS	37
5.2	Resonator central strip and the gap	38
5.3	Pad and coupling capacitor	38
5.4	Perfectly conducting ground plane and resonator	38
5.5	Lumped ports	39
5.6	Radiation boundary around the resonator	39
5.7	Resultant mesh after convergence	40
5.8	S21 parameter	41
5.9	Resonant frequency	41
5.10	Ar:N=10:6 at 3mTorr, $T_c = 12K$	42
5.11	Ar:N=10:8 at 3mTorr, $T_c = 12.2K$	43
5.12	Ar:N=10:10 at 3mTorr	43
5.13	Final result after all the fabrication	44
5.14	Transmission amplitude vs Frequency or S21	45
5.15	Phase vs Frequency	45

Chapter 1

Introduction

1.1 Spin qubits and long-distance qubit coupling

A qubit is a two-level system. There are several ways of making an artificial or a natural two level system. One of the ways of making a very natural two-level system is by controlling the spin of a single electron [4]. This can be done by isolating an electron inside a magnetic field. In the presence of the magnetic field the electron's spin 1/2 states split into two states with energy difference $E_Z = g\mu_B B$, where g is the electron g-factor, μ_B is the Bohr magneton and B is the magnetic field. If we isolate N electrons we can get N qubits by applying a global magnetic field and controlling their spins.

In order to isolate single electrons, the electron has to be confined in an electrostatic potential on sub-micron length scales. This is done using a Quantum Dot. The first Quantum Dots were made on GaAs/AlGaAs devices [5], but the majority of them are now made on silicon [6] because of existing semiconductor fabrication technologies that with slight modifications can be employed to make quantum dots.

As we can see from Figure 1.1(a), to isolate electrons we can place them inside the conduction band of the silicon quantum well (Si QW) in between the SiGe spacer and SiGe buffer. This will restrict any free electrons vertically in the quantum well. This is known as a heterostructure. A thin layer of silicon is deposited on top of it to prevent the substrate from oxidising. The control of the electrons in the quantum dot is achieved by fabricating three layers of aluminium electrodes on top of the Si cap [7], as shown in Figure 1.1(b). These electrodes form the gates and every one of them is isolated from the other by a thin layer of aluminium oxide. Different electrodes have different functionalities, such as, the S_1, S_2 (source) and D_1, D_2 (drain) gates accumulate electrons from a separately doped region, the electrons are stabilised inside by the red coloured gates that form a local potential minima where small islands of electrons can be formed. This island is the quantum dot.

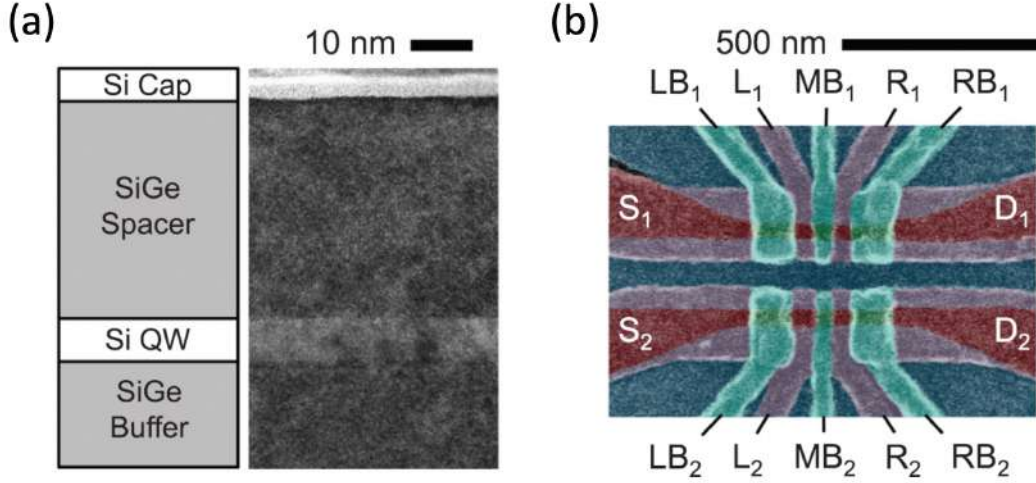


Figure 1.1: (a) Cross-section of Si/SiGe heterostructures that confine electrons in the vertical direction. Left: Schematic of the heterostructure. Right: TEM of a heterostructure. (b) False coloured SEM of a double quantum dot(DQD)

To model a quantum dot we can think of it as a collection of several capacitors. Its total energy is given by

$$U(N) = \frac{(-|e|N + C_S V_S + C_D V_D + C_G V_G)^2}{2C} + \sum_{n=1}^N E_n(B) \quad (1.1)$$

where N is the number of electrons in the quantum dot, C_S, C_D, C_G are the capacitances between the quantum dot and the source, drain and gate respectively, V_S, V_D, V_G are the voltages applied to them and $C = C_S + C_D + C_G$, $E_n(B)$ is the energy of the single electron state inside the quantum dot which includes the orbital, spin state and valley energies and it depends on the magnetic field B [8].

The energy required to add the N^{th} electron to the quantum dot is

$$\mu_N = U(N) - U(N-1) = \left(N - \frac{1}{2}\right) E_C - \frac{E_C}{|e|} (C_S V_S + C_D V_D + C_G V_G) + E_n(B) \quad (1.2)$$

where $E_C = e^2/C$ [8].

As stated before, once we isolate the electrons inside the quantum dot, its spin state can be controlled by applying magnetic fields. If these magnetic fields are in resonance then they will drive Rabi oscillations of the spin. This will cause the electrons to rotate periodically between the spin up and the spin down states. In the Bloch sphere, this corresponds to controlling the angle θ . Additional control of the quantum dot is necessary to control the angle ϕ .

The spin interacts with its environment very weakly as compared to the charge. This naturally leads to very long coherence times for spin qubits. Coherence times of up to 28 ms have been observed. This has enabled us to make high fidelity single qubit gates. This is in contrast to superconducting qubits. But when it comes to implementing two qubit gates, using the spin of the electron as a qubit becomes an issue as the small footprint of the spatial distribution of the electron wavefunction prevents the overlap of wavefunctions of two electrons, when they are separated by a large distance, which makes it harder for two qubits to interact with each other. So implementing two qubit gates is practically possible only with electrons in neighbouring quantum dots [9], typically within 100 nm of each other. Whereas, superconducting qubits can be coupled very easily over mm length scale using circuit quantum electrodynamics [10]. In this thesis, we are going to extend the same concept to couple two spin qubits separated by a long distance to enable high fidelity two qubit gates.

1.2 Spin photon coupling

Two spin qubits separated by a long distance are coupled to each other via a cavity that consists of photons, or in other words an optical cavity. For two qubits to couple to each other, both the qubits first have to couple to the optical cavity. Let us try to understand how a qubit and an optical cavity couple to each other.

The spin qubits are two level systems or it can also be said that they are artificial two level atoms. This two level atom can interact with a quantized mode of an optical cavity. This interaction is described by Jaynes Cummings Hamiltonian [11].

$$H_{JC} = H_{cavity} + H_{atom} + H_{int} = \hbar\omega_r(a^\dagger a + 1/2) + \hbar\frac{\omega_a}{2}\sigma_z + \hbar g(a^\dagger\sigma^- + a\sigma^+) \quad (1.3)$$

Here the first term, H_{cavity} , describes the quantised optical cavity fields with resonance frequency ω_r , a^\dagger and a are photon creation and annihilation operators. The second term, H_{atom} , describes the two level atom, or an atom in which only two states are accessible. ω_a is the resonance frequency of the atom such that $\hbar\omega_a$ is the energy difference between the two accessible states, σ_z is the Pauli Z operator. The last term, H_{int} , describes the interaction or coupling between the two systems. It says that when the two level atom and the quantised optical cavity are coupled to each other then an annihilation of a photon in the cavity leads to the excitation of the atom or the de-excitation of the atom leads to the creation of a photon in the cavity. The study of this phenomenon is known as Cavity Quantum Electrodynamics.

The interaction of the atom with the cavity is actually the interaction of the dipole formed by the atom and the electric field inside the cavity. The first demonstrations

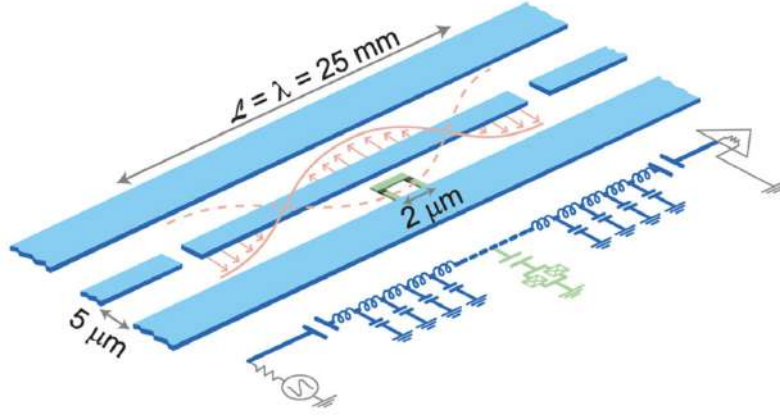


Figure 1.2: Schematic of a typical coplanar waveguide to couple superconducting qubits

of this were done by dropping Cesium atoms or highly excited Rydberg atoms into a cavity, the dipole formed by the atomic nucleus and its outer electrons interacts with the electromagnetic field in the cavity. When the coupling between the two systems was strong enough such that it compensated the rate at which either the photon leaks out of the cavity or the atomic excitation decays on its own, the photon excited the atom and caused an oscillation between a cavity excitation and an atom excitation. After these experiments, research efforts were focused on to replacing these atoms with artificial atoms whose properties could be much more easily controlled, which will help us in scaling toward larger systems. This led to the birth of Circuit Quantum Electrodynamics, by making artificial atoms or two level systems with superconducting circuits that usually consist of inductors, capacitors and Josephson junctions [12]. In our case, the artificial atoms or two level systems are made by isolating an electron inside a quantum dot and applying a strong magnetic field to it. These two level systems are easily designed and fabricated on top of a flat substrate using various lithography techniques, the cavities are also implemented with two dimensional coplanar waveguide resonators, Figure 1.2.

1.3 Fundamentals of Microwave Resonators

1.3.1 Theory for Transmission lines

To understand microwave resonators we first need to understand transmission line theory. We use these concepts to develop a theory for resonators.

Transmission lines almost always have two conductors. Hence, they are represented as a two wire line. Let us consider an infinitesimal piece of a transmission line of length Δz and model it as a lumped element circuit, as shown in Figure 1.3(b). Here R is the series resistance per unit length (Ω/m), L is the series inductance per unit length (H/m), G is the shunt conductance per unit length (S/m) and C is the shunt capacitance per

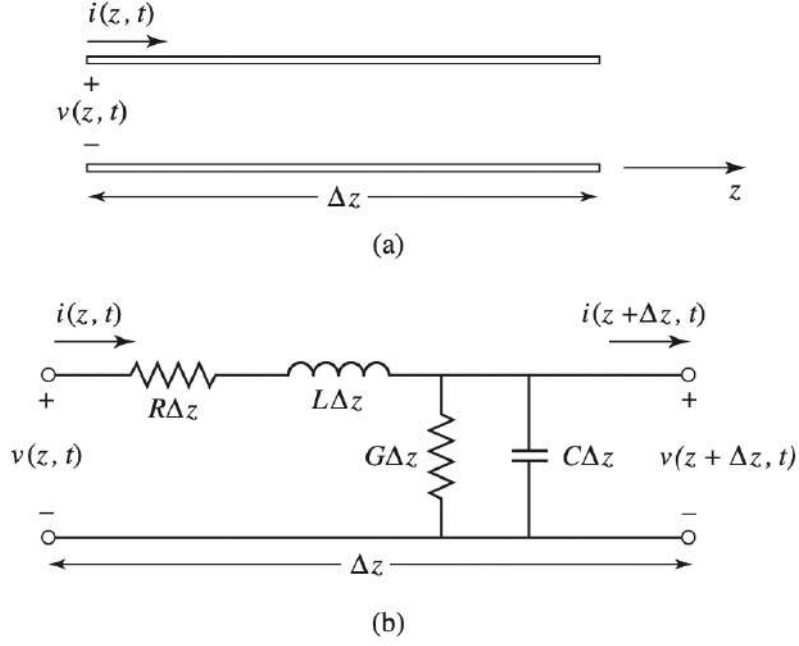


Figure 1.3: (a) Transmission line representation and its voltage and current (b) Equivalent lumped element circuit

unit length(F/m). R is due to the finite conductivity of the conductors, L represents the total self-inductance of the conductors, G is due to dielectric loss in the material between the conductors and C is due to the close proximity of the two conductors.

In the lumped element equivalent circuit applying Kirchoff's voltage law gives us

$$v(z, t) - R\Delta z i(z, t) - L\Delta z \frac{\partial i(z, t)}{\partial t} - v(z + \Delta z, t) = 0 \quad (1.4)$$

and applying Kirchoff's current law gives us

$$i(z, t) - G\Delta z v(z + \Delta z, t) - C\Delta z \frac{\partial v(z + \Delta z, t)}{\partial t} - i(z + \Delta z, t) = 0 \quad (1.5)$$

Dividing 1.3 and 1.4 by Δz and taking the limit $\Delta z \rightarrow 0$ gives us

$$\begin{aligned} \frac{\partial v(z, t)}{\partial z} &= -Ri(z, t) - L \frac{\partial i(z, t)}{\partial t} \\ \frac{\partial i(z, t)}{\partial z} &= -Gv(z, t) - C \frac{\partial v(z, t)}{\partial t} \end{aligned} \quad (1.6)$$

These are known as the Telegrapher's equations.

Assuming sinusoidal steady state condition, i.e. $i(z, t) = I(z)e^{j\omega t}$ and $v(z, t) = V(z)e^{j\omega t}$, we get

$$\begin{aligned}\frac{dV(z)}{dz} &= -(R + j\omega L)I(z) \\ \frac{dI(z)}{dz} &= -(G + j\omega C)V(z)\end{aligned}\tag{1.7}$$

Solving the two equations simultaneously will give us wave equations for $V(z)$ and $I(z)$

$$\begin{aligned}\frac{d^2V(z)}{dz^2} - \gamma^2 V(z) &= 0 \\ \frac{d^2I(z)}{dz^2} - \gamma^2 I(z) &= 0\end{aligned}\tag{1.8}$$

where

$$\gamma = \alpha + j\beta = \sqrt{(R + j\omega L)(G + j\omega C)}\tag{1.9}$$

is the complex propagation constant that depends on frequency ω . The attenuation constant α is a sum of four different components

$$\alpha = \alpha_C + \alpha_D + \alpha_G + \alpha_R\tag{1.10}$$

α_C represents loss due to finite metal conductivity, α_D is dielectric loss tangent, α_G is conductivity loss of the dielectric and α_R is radiation loss.

Solving equations(1.7) gives us traveling wave solutions

$$\begin{aligned}V(z) &= V_0^+ e^{-\gamma z} + V_0^- e^{\gamma z} \\ I(z) &= I_0^+ e^{-\gamma z} + I_0^- e^{\gamma z}\end{aligned}\tag{1.11}$$

where $e^{-\gamma z}$ component propagates in $+z$ direction and $e^{\gamma z}$ component propagates in the $-z$ direction.

Substituting the voltage equation from (1.11) into (1.7) we get

$$I(z) = \frac{\gamma}{R + j\omega L} (V_0^+ e^{-\gamma z} - V_0^- e^{\gamma z})\tag{1.12}$$

We define characteristic impedance, Z_0 , as

$$\begin{aligned}Z_0 &= \frac{R + j\omega L}{\gamma} = \sqrt{\frac{R + j\omega L}{G + j\omega C}} \\ Z_0 &= \frac{V_0^+}{I_0^+} = \frac{-V_0^-}{I_0^-}\end{aligned}\tag{1.13}$$

Therefore, (1.9) can be written as

$$\begin{aligned} V(z) &= V_0^+ e^{-\gamma z} + V_0^- e^{\gamma z} \\ I(z) &= \frac{V_0^+}{Z_0} e^{-\gamma z} - \frac{V_0^-}{Z_0} e^{\gamma z} \end{aligned} \quad (1.14)$$

Lossless line

In practical situations, the loss of the line is very small and can be neglected. Setting $R = G = 0$ in the above equations gives us

$$\gamma = j\omega\sqrt{LC} \quad (1.15)$$

or

$$\alpha = 0 \quad \beta = \omega\sqrt{LC} \quad (1.16)$$

the attenuation constant is zero.

The characteristic impedance becomes

$$Z_0 = \sqrt{\frac{L}{C}} \quad (1.17)$$

The voltage and current wave equations for the lossless line are

$$\begin{aligned} V(z) &= V_0^+ e^{-j\beta z} + V_0^- e^{j\beta z} \\ I(z) &= \frac{V_0^+}{Z_0} e^{-j\beta z} - \frac{V_0^-}{Z_0} e^{j\beta z} \end{aligned} \quad (1.18)$$

1.3.2 Terminated Lossless Transmission line

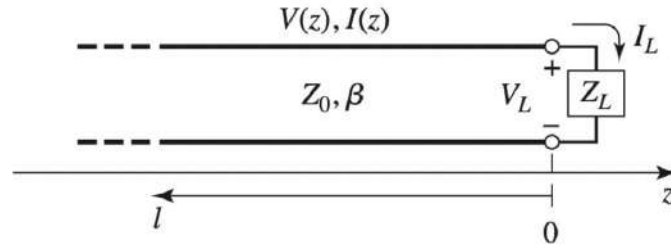


Figure 1.4: Transmission line terminated with load impedance Z_L

Figure 1.3 illustrates a terminated transmission line. A wave of the form V_0^+ is incident from $z < 0$. The transmission line has a characteristic impedance Z_0 , but it terminates at a load $Z_L \neq Z_0$. Thus a reflected wave should be present so that the ratio of the voltage and current at $z = 0$ is equal to Z_L .

The total voltage on the line is

$$V(z) = V_0^+ e^{-j\beta z} + V_0^- e^{j\beta z} \quad (1.19)$$

and the total current on the line is

$$I(z) = \frac{V_0^+}{Z_0} e^{-j\beta z} - \frac{V_0^-}{Z_0} e^{j\beta z} \quad (1.20)$$

At $z = 0$

$$Z_L = \frac{V(0)}{I(0)} = \frac{V_0^+ + V_0^-}{V_0^+ - V_0^-} Z_0 \quad (1.21)$$

rearranging this gives

$$V_0^- = \frac{Z_L - Z_0}{Z_L + Z_0} V_0^+ \quad (1.22)$$

The voltage reflection coefficient, Γ , is defined as the amplitude of the reflected voltage divided by the incident voltage

$$\Gamma = \frac{V_0^-}{V_0^+} = \frac{Z_L - Z_0}{Z_L + Z_0} \quad (1.23)$$

Hence, the total voltage and current on the line becomes

$$\begin{aligned} V(z) &= V_0^+ (e^{-j\beta z} + \Gamma e^{j\beta z}) \\ I(z) &= \frac{V_0^+}{Z_0} (e^{-j\beta z} - \Gamma e^{j\beta z}) \end{aligned} \quad (1.24)$$

Looking toward the load from $Z = -l$ the input impedance is

$$Z_{in} = \frac{V(-l)}{I(-l)} = Z_0 \frac{Z_L + jZ_0 \tan(\beta l)}{Z_0 + jZ_L \tan(\beta l)} \quad (1.25)$$

When the line is open from the end, i.e. $Z_L = \infty$, as shown in Figure 1.4, $\Gamma = 1$ and the input impedance is

$$Z_{in} = -jZ_0 \cot(\beta l) \quad (1.26)$$

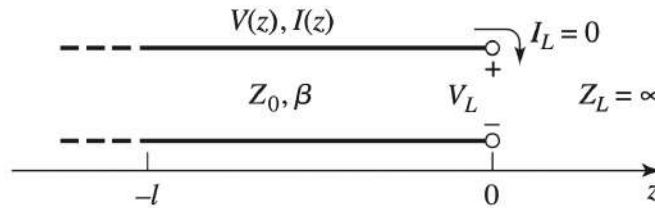


Figure 1.5: Transmission line terminated with open circuit

1.3.3 Transmission line resonators

The co-planar waveguide resonators are open circuited $\lambda/2$ transmission line resonators. Near resonance, these types of resonators are modeled as a parallel RLC circuit [13]. So let us first try to understand parallel RLC circuits.

Parallel RLC circuit

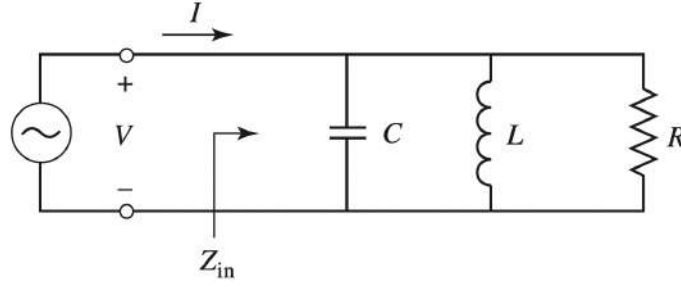


Figure 1.6: A parallel RLC circuit

The input impedance is

$$Z_{in} = \left(\frac{1}{R} + \frac{1}{j\omega L} + j\omega C \right)^{-1} \quad (1.27)$$

The input power is given by [13]

$$\begin{aligned} P_{in} &= \frac{1}{2} V I^* = \frac{1}{2} |V|^2 \frac{1}{Z_{in}^*} \\ &= \frac{1}{2} |V|^2 \left(\frac{1}{R} + \frac{j}{\omega L} - j\omega C \right) \end{aligned} \quad (1.28)$$

The power dissipation due to the resistor is

$$P_{loss} = \frac{1}{2} \frac{|V|^2}{R} \quad (1.29)$$

Let W_m be the magnetic energy stored in the inductor and W_e be the electric energy stored in the capacitor. Their expressions are given by

$$\begin{aligned} W_m &= \frac{1}{4} |V|^2 \frac{1}{\omega^2 L} \\ W_e &= \frac{1}{4} |V|^2 C \end{aligned} \quad (1.30)$$

The input power can then be written as [13]

$$P_{in} = P_{loss} + 2j\omega(W_m - W_e) \quad (1.31)$$

The resonant frequency, ω_0 , is the frequency at which $W_m = W_e$ which implies that

$$\omega_0 = \frac{1}{\sqrt{LC}} \quad (1.32)$$

The quality factor, Q of a resonant circuit is defined as [13]

$$\begin{aligned} Q &= \omega \frac{\text{average energy stored}}{\text{average loss per second}} \\ &= \omega \frac{W_m + W_e}{P_{loss}} \end{aligned} \quad (1.33)$$

and for a parallel RLC circuit at resonance, the unloaded Q is expressed as

$$Q_0 = \omega_0 \frac{2W_m}{P_{loss}} = \frac{R}{\omega_0 L} = \omega_0 RC \quad (1.34)$$

Near the resonance, i.e. when $\omega = \omega_0 + \Delta\omega$ where $\Delta\omega$ is small, the input impedance becomes

$$Z_{in} = \frac{R}{1 + 2j\Delta\omega RC} \quad (1.35)$$

Open circuited $\lambda/2$ line

We generalise and consider a lossy transmission line whose length is $l = n\lambda/2$ with n as the resonant mode number. It behaves as a parallel RLC circuit.

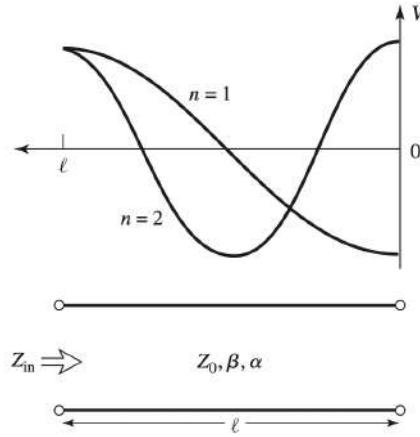


Figure 1.7: An open circuited lossy transmission line and its voltage distributions for $n = 1$ and $n = 2$

The input impedance is [13]

$$Z_{in} = Z_0 \coth(\alpha + j\beta)l = Z_0 \frac{1 + j \tan(\beta l) \tanh(\alpha l)}{\tanh(\alpha l) + j \tan(\beta l)} \quad (1.36)$$

At resonance, i.e. $\omega = \omega_0$, $l = \lambda/2$. Let $\omega = \omega_0 + \Delta\omega$, then

$$\beta l = \frac{\omega}{v_p} \frac{\lambda}{2} = \frac{(\omega_0 + \Delta\omega)}{v_p} \frac{\pi v_p}{\omega_0} = \pi + \frac{\Delta\omega\pi}{\omega_0} \quad (1.37)$$

so

$$\tan(\beta l) = \tan\left(\frac{\Delta\omega\pi}{\omega_0}\right) \approx \frac{\Delta\omega\pi}{\omega_0} \quad (1.38)$$

and

$$\tanh(\alpha l) \approx \alpha l \quad (1.39)$$

substituting (1.37) and (1.38) into (1.35) we get

$$Z_{in} = \frac{Z_0}{\alpha l + j(\Delta\omega\pi/\omega_0)} \quad (1.40)$$

Comparing with the input impedance of the parallel RLC circuit, (1.34), we can see that the resistance, capacitance and inductance of the equivalent RLC circuit is

$$R = \frac{Z_0}{\alpha l} \quad C = \frac{\pi}{2\omega_0 Z_0} L = \frac{1}{\omega_0^2 C} \quad (1.41)$$

and hence the unloaded Q is

$$Q_0 = \omega_0 RC = \frac{\pi}{2\alpha l} = \frac{\beta}{2\alpha} \quad (1.42)$$

Quality factor of a resonator

The quality factor gives us the relation between the stored energy and the dissipated energy and is a very important factor. It is connected to the sharpness of the resonant frequency. In the preceding sections, we defined the unloaded Q, Q_0 . It is valid only in the absence of any loads, i.e the resonator is not connected to any external circuitry, hence it is a characteristic of the resonator itself. In practice, the resonator is always connected to other circuits that will lower the Q, called loaded Q, Q_L , of the circuit. If we define the quality factor of the external circuit as Q_e then Q_L is

$$\frac{1}{Q_L} = \frac{1}{Q_e} + \frac{1}{Q_0} \quad (1.43)$$

Coupling

There is something called zero point voltage fluctuations $V_{ZPF} \propto f_0 \sqrt{Z_0}$, where f_0 is the resonator fundamental frequency, of a resonator that needs to have a very large value for the microwave photons in the resonator to couple with the small electric dipole moments of the spin qubits. This can be achieved by increasing the value of Z_0 [1], and since $Z_0 = \sqrt{L/C}$, making the inductance of the resonator very high does the job.

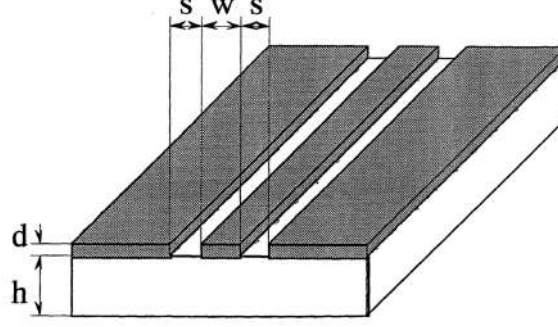


Figure 1.8: Coplanar waveguide dimensions

Now $L = L_m + L_k$, where L_m is the usual magnetic inductance, which depends only on the structure, and L_k is the kinetic inductance, which depends both on the structure and the material. In the case of thin films, using which we fabricate our resonators, L_k dominates over L_m by a huge amount. So to achieve high Z_0 we fabricate resonators using materials with very high kinetic inductance, such as NbN or NbTiN. Doing this enhances the coupling strength.

Kinetic inductance

It is a phenomenon that behaves exactly like the usual inductance but has its origins in the kinetic energy of the moving electrons inside the metal instead of magnetism. It only comes into existence in superconductors. For coplanar waveguide resonators, the formula for kinetic inductance is given by [14]

$$L_k = \mu_0 \frac{\lambda^2}{dw} g(s, w, d) \quad (1.44)$$

$$g(s, w, d) = \frac{1}{2k^2 K(k)^2} \left[-\ln \frac{d}{4w} - \frac{w}{w+2s} \ln \frac{d}{4(w+2s)} + \frac{2(w+s)}{w+2s} \ln \frac{s}{w+s} \right]$$

where $k = w/(w+2s)$, $K(k)$ is the complete elliptical integral of the first kind, λ is the magnetic penetration depth, d is the film thickness, w is the width of the central electrode and s is the spacing between the grounded electrode and the central electrode as can be seen from Figure 1.8.

Chapter 2

Background work

Nano electronics group, University of Basel, Switzerland

They have made 10 nm thick films of NbN at several temperatures with the following properties

Temperature (°C)	R_{\square} ($\Omega \square^{-1}$)	T_c (K)	Kinetic inductance ($\text{pH} \square^{-1}$)
275	273	10.5	36
275	339	9.6	49
180	480	7.7	86
180	550	7.4	103
22	670	5.9	162
22	705	5.6	174

Figure 2.1: NbN film characterization for different sputtering temperatures [1]

Increasing the T_C increases the critical magnetic field, H_C , and hence the film would remain superconducting at higher temperatures, but doing that decreases the kinetic inductance. So the group went with a trade off and decided to use the film with $T_C = 7.4K$ [1].

To measure the kinetic inductance of their resonator they first reconstructed its dispersion relation by measuring several of its resonant frequencies using a vector network analyser. The wave is just $k = n\pi/l$, where l is the length of resonator and n is the resonance mode. The relation between these two quantities and the kinetic inductance is known [1],

$$v_{ph} = \frac{\omega_n}{k_n} = \frac{1}{\sqrt{C(L_m + L_k)}} \quad (2.1)$$

where C is the capacitance and L_m is the magnetic inductance of the resonator which only depends on its dimensions and can be calculated using conformal mapping calculations. From the above formula, L_k can be calculated.

They then designed three resonators with the properties given in Figure 2.2.

Z_c	110 Ω	890 Ω	4.1 k Ω
s (μm)	50	2	0.2
w (μm)	2	2	2

Figure 2.2: Characteristic impedance of resonators with different designs [1]

where s is the width of the central conductor and w is the gap on the two sides of the central conductor.

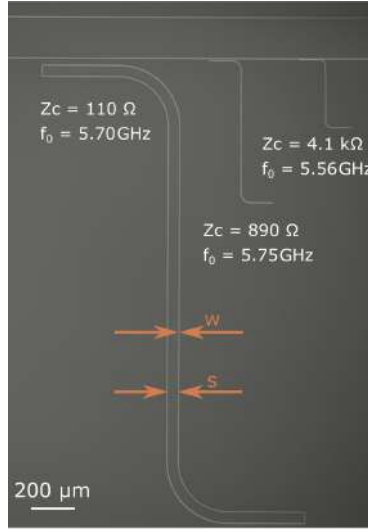


Figure 2.3: SEM images of the three resonators [1]

They also calculated the quality factors of the three resonators and achieved a quality factor $> 10^4$ for the resonator with $Z_C = 4.1k\omega$, in the single photon regime.

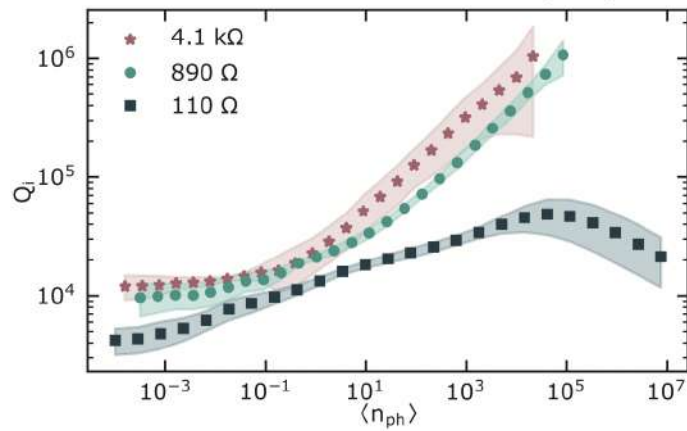


Figure 2.4: Internal quality factor, Q_i vs the average photon number inside the resonator, $\langle n_{ph} \rangle$ for the three resonators [1]

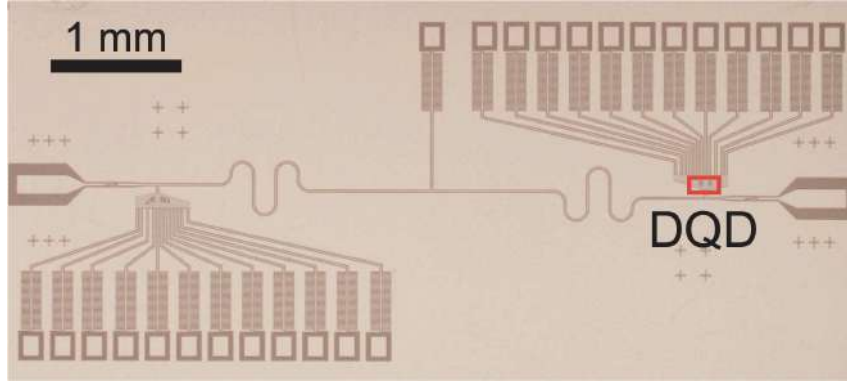


Figure 2.5: Optical image of the resonator and the two double quantum dots at its ends [2]

Their resonator is made from Nb and consists of two gate defined Si DQD(Double Quantum Dot). The resonant frequency of the resonator was $f_c = 7.684\text{GHz}$ with a loaded quality factor $Q_c = 7460$ [2]. The width of the central conductor in their design is 600nm and the width of the gap on the two sides of the central conductor is $20\mu\text{m}$.

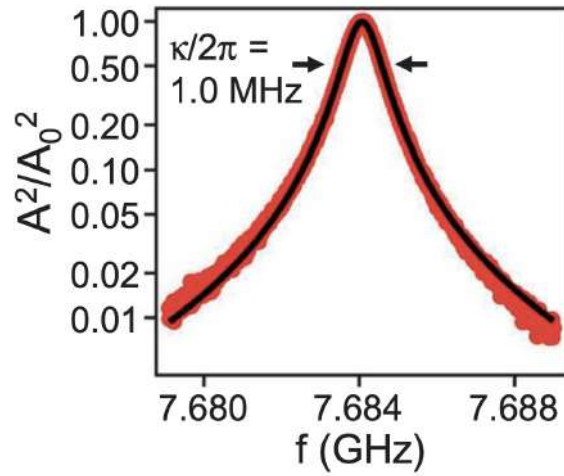


Figure 2.6: Square of the ratio of the transmitted amplitude to the incident amplitude of the microwave vs frequency of the microwave [2]

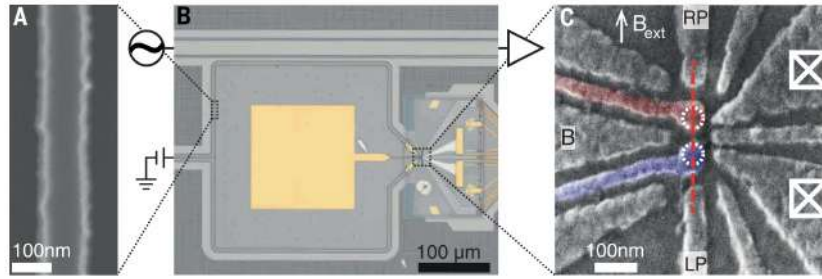


Figure 2.7: (A) SEM image of the centre conductor of the resonator, (B) Optical micrograph of the resonator, (C) SEM of the double quantum dot [3]

In their design, the width of centre conductor is 100nm . It is made from NbTiN thin film and has a characteristic impedance of $1k\Omega$. They have achieved a resonance frequency of 6.051GHz [3].

Chapter 3

Methodology and Processes

3.1 Sputtering

Sputtering, in simple words, is a process where we scoop material from the surface literally atom by atom by shooting certain kinds of little projectiles. And in the process, those scooped out atoms will travel towards the substrate and deposit onto it. This is how we create thin films. Now let us try to understand it in detail [15].

We have an enclosed chamber, with an air pressure of the order of 10^{-8} or 10^{-9} Torr, i.e. it has a high vacuum. As a result, there are no reactive gases inside the chamber. We place the substrate, on which we want the thin film to be deposited, on top of the chamber facing upside down. The material that is to be deposited sits underneath the substrate facing it, this is called the target. The substrate and the target are connected to each other using an electrical circuit. The target is connected to the negative electrode of the circuit and the substrate is connected to the positive electrode. When the process needs to be done, the chamber is filled with Argon gas and maintained at a pressure of 3 mBar to 30 mBar during the process. Argon gas is used because it is nonreactive. A very high voltage is maintained across the positive and the negative electrodes, i.e. across the substrate and the target respectively. Because of this voltage, the Argon gas ionises and creates a plasma. Now the positively charged Argon ions get attracted towards the negative electrode, i.e. towards the target. Because of the voltage they accelerate and hit the target at very high speeds. This collision gives the atoms of the target enough energy to leave the surface and still carry enough energy to keep moving towards the substrate. These atoms then collide with the surface and get deposited on it. This process goes on and a layer of the target keeps forming on the surface of the substrate. The longer it goes on, the thicker would be the film. This is the process of Sputtering.

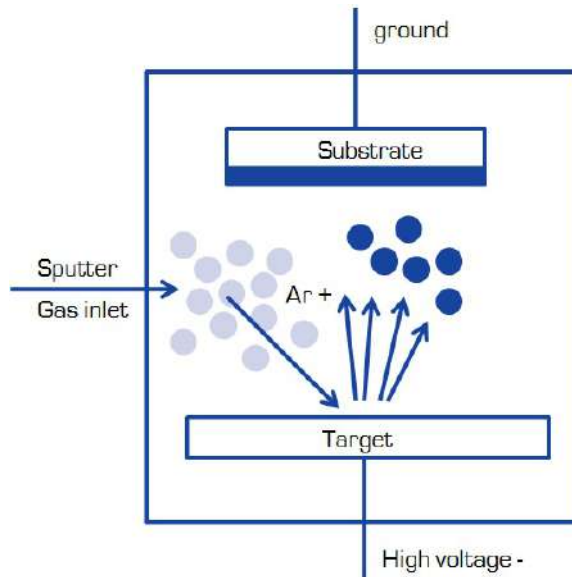


Figure 3.1: Sputter deposition

Types of Sputtering

1. DC Sputtering - In this type of sputtering a DC current is used to create the plasma between the substrate and the target.
2. RF Sputtering - In this type of sputtering an AC current is used to create the plasma between the substrate and the target. This is used in those cases when the target is a non conducting material. The rate of film deposition is slower compared to DC Sputtering.

The Argon gas keeps on flowing at a certain rate to maintain a fresh supply of Argon gas to create the plasma and to knock out the target atoms. The flow rate is measured in sccm(standard cubic centimeter per minute) and in our system, it is kept at a fixed value of 10 sccm.

Along with flowing Argon gas, we can also flow other gases such as Nitrogen or Oxygen. The process is then known as reactive sputtering in which the target atoms when on the way to the substrate react with these additional gas(es) to create nitrides or oxides and then deposit on the substrate. For example to create NbN thin films an Nb target is used with Nitrogen gas flowing inside the chamber.

Aspect	Photolithography	EBL
<i>Wavelength/spot-size</i>	$\approx 300 \text{ nm}$	$\approx 2 \text{ nm}$
<i>Minimum feature size</i>	$\approx 0.5 \text{ }\mu\text{m}$	$\approx 6 \text{ nm}$
<i>Alignment accuracy</i>	$> 1 \text{ }\mu\text{m}$	$> 6 \text{ nm}$
<i>Wafer exposure speed</i>	Whole wafer at once Fast: Minutes	Serial scanning beam Very slow: hours

Figure 3.2: Comparison of various aspects of Electron Beam Lithography(EBL) and Photolithography

3.2 Electron Beam Lithography

Lithography essentially is a process of printing. In terms of semiconductors, it is a process using which we draw circuit patterns and elements on the substrate.

In optical lithography, a light-sensitive polymer, called a photoresist, is exposed and developed to form 3D images or patterns on the substrate.

Electron beam lithography is a similar process in which we expose the resist to an electron beam instead of light to create patterns on the substrate. It is considerably more complicated and slower than optical lithography. Then why use electron beam lithography? The answer is, to increase the resolution. The resolution of patterns we can expose is limited by the wavelength of the beam we use. Since electrons have a much smaller wavelength than light, the resolution achieved by electron beam lithography is much higher than what is achieved by photolithography.

The wavelength of an electron is given by the de Broglie equation

$$\lambda = \frac{h}{p} \quad (3.1)$$

where h is Planck's constant and p is the momentum of the electron. The electrons are accelerated to a very high velocity by an electric potential U . Its wavelength, considering the relativistic effects, is given by

$$\lambda = \frac{h}{\sqrt{2m_0eU}} \frac{1}{\sqrt{1 + \frac{eU}{2m_0c^2}}} \quad (3.2)$$

where c is the speed of light. The wavelength of electron when $U = 10kV$ is $12.3pm$ and when $U = 200kV$ it is $2.5pm$.

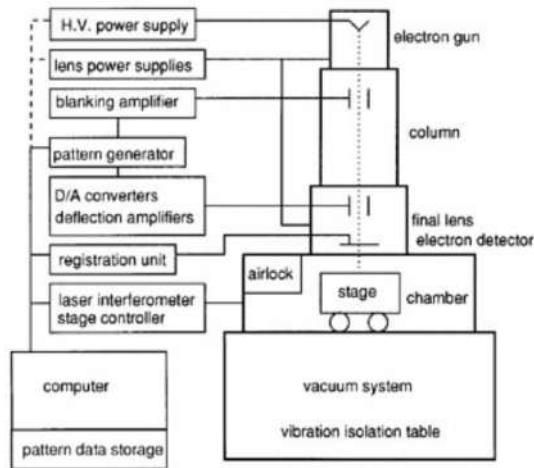


Figure 3.3: Microscope column of an EBL

How electron beam lithography works

The EBL machine consists of a microscope column, Figure 3.3, which generates the electron beam and focuses it on to the specimen. It has the following parts [16]

- The electron gun produces an electron beam
- Several condenser and objective lenses to control the diameter of the beam and focus the beam on the substrate.
- A deflector to move the beam over the surface of the substrate. It can be either magnetic or electrostatic.
- A beam blanker to turn off the beam.
- Several apertures to control the diameter and hence current of the beam.
- A laser interferometer to help in loading, unloading and moving the sample around inside the chamber.
- A vacuum system to maintain high vacuum levels (up to 2×10^{-9} mBar) throughout the column.

When a beam hits the surface of the resist it interacts with the electrons in the resist. The incoming electrons transfer their energy to these electrons inside the resist. This results in the expulsion of these electrons from their atoms that carry energy, typically, less than 50eV. This is an inelastic event and these electrons are known as secondary electrons [16]. Another thing that can happen when the electron beam hits the surface of the resist is that the incoming electron just interacts with the electric field of the atoms without much change in its energy, it only results in a change of its direction. These

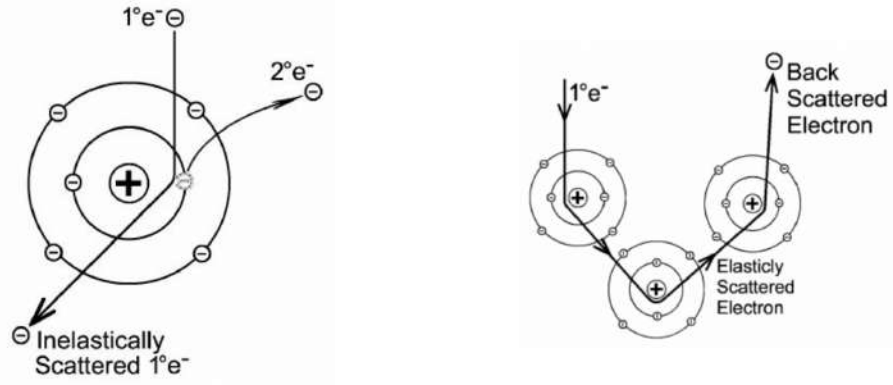


Figure 3.4: The inelastic and elastic scattering of the electron beam on interaction with resist

electrons deflect back out of the specimen and are known as backscattered electrons. This is an elastic event and these electrons can have energies from 50eV to nearly the incident beam energy [16]. These electrons change the chemical properties of the resist, more precisely, it changes the solubility of the resist and hence the resist either becomes more soluble in a chemical or less soluble than before which then causes the resist to be selectively removed from the substrate during the process known as development.

3.3 Reactive Ion Etching

Reactive ion etching (RIE) is a dry etching process that is often used in the semiconductor manufacturing, microfabrication industries and nanotechnology research to create precise patterns on surfaces. In RIE, reactive ions are used to remove material from a substrate. The process involves several steps. First, a substrate is placed in a vacuum chamber and exposed to a gas mixture, usually consisting of a noble gas such as argon and a reactive gas such as oxygen or fluorine. The gas is ionized by applying a radio frequency or microwave energy, which creates a plasma.

The plasma consists of positive ions, negative ions, and free electrons. The positive ions are accelerated towards the substrate by an electric field, where they collide with and remove material from the surface. The negative ions and free electrons can also participate in the process by reacting with or neutralizing the positive ions, or by modifying the surface chemistry.

The etching rate and the ratio of etch rates between materials, also known as, selectivity of RIE depend on several factors, such as the gas composition, pressure, power, and temperature. The gas composition determines the chemistry of the plasma and the types of products that are generated. For example, oxygen can react with metals to form metal oxides, while fluorine can form volatile fluorides. The pressure affects the density and energy of the plasma, as well as the mean free path of the ions. Higher pressure can increase the ion bombardment and improve the uniformity of the etching. The power controls the

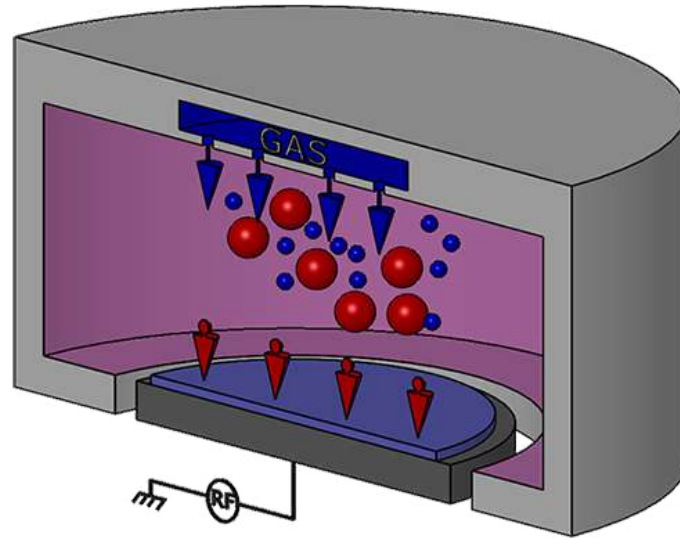


Figure 3.5: Diagram showing Reactive Ion Etching process

intensity of the plasma and the density of the ions. Higher power can increase the etching rate, but also increase the risk of damage or heating to the substrate. The temperature affects the surface chemistry and the etch rate, as well as the stress and deformation of the substrate.

It can be used for a variety of applications, such as etching of Silicon dioxide, Niobium Nitride, and metals, as well as pattern transfer and plasma doping. It offers several advantages over wet etching, such as higher selectivity, better control of the profile and depth, and lower contamination and waste. However, it also has some limitations, such as the need for specialized equipment and expertise, the potential for damage or roughening of the surface, and the possibility of ion-induced damage or implantation.

Chapter 4

Troubleshooting

This chapter includes all the details about the fabrication process and their optimisation.

4.1 Fabrication process

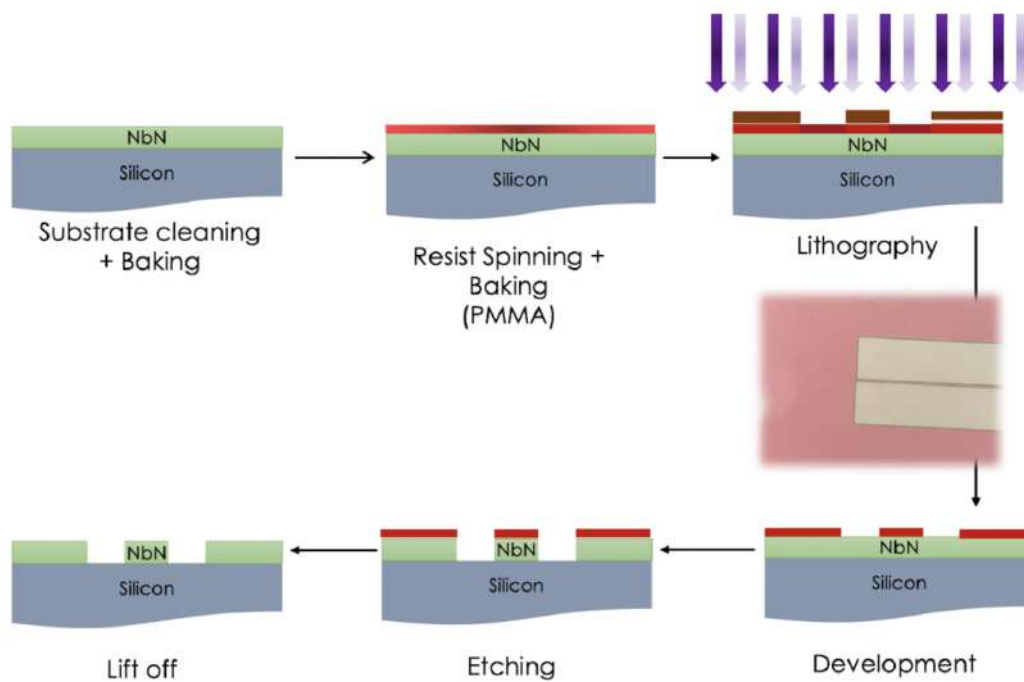


Figure 4.1: Overview of all the fabrication processes required to make the resonator

4.2 Lithography

I have divided the progress into the issues I faced and their solutions, each month.

October

- Since we need a central line that is of very long length and of uniform thickness we cannot afford to have stitching errors which will change the thickness at the boundaries of write field. To avoid that, i.e. write without stitching errors, Raith150Two provides a method called Fixed Beam Moving Stage(FBMS).
- I obtained almost perfect central strip using FBMS mode but there were stitching errors, this definitely meant that the writing was not being done using FBMS mode even after selecting it.

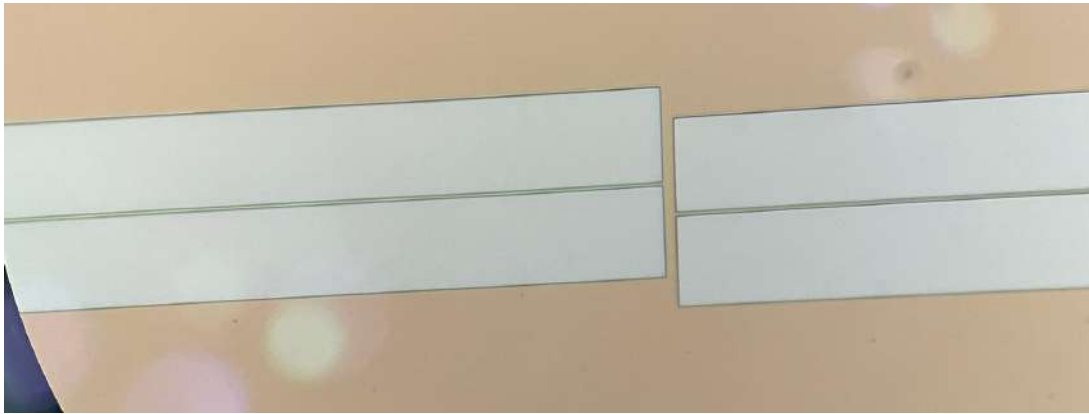


Figure 4.2: Stitching error

- Another sign was that when starting the exposure, the software always gave me an error that 'FBMS line elements was not selected'.
- This was happening because of the gds file. FBMS only supports line and curved elements and they are needed to be drawn using the raith software by especially selecting "draw fbms elements". There is also another option of converting normal elements into fbms elements.
- I was doing the latter but it was not properly converting the elements. I had two rectangles, when converting it was only converting the edges of the rectangle into fbms line elements and leaving the area as normal mode.
- So, I understood that fbms only recognizes line elements and not any other shapes. To make rectangles I first drew lines and then changed their line width to 20 microns. Converting into fbms elements after doing this worked perfectly.
- No stitching error was observed after doing this.

November

- Once I started using FBMS mode, the two rectangles that I was making to get the central strip were not properly exposed. The exposure time was very less and

not changing no matter the current value and the dose value. This was happening because the stage speed was very high, I noticed this particular fact only at a very later stage.

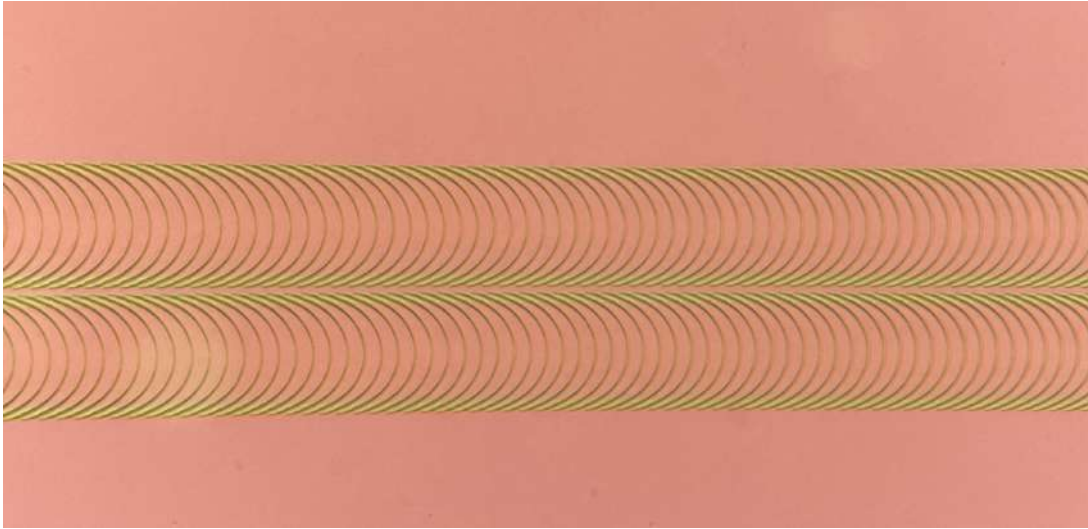


Figure 4.3: Improper exposure

- This was surprisingly resolved by using my own account on the Raith software instead of using the training account, which is the default account.
- This seems very weird now, and it is weird. Actually, there is an underlying bug that is causing all of this, it will come back to haunt us later and I will realise what it is only then.

December

- I was getting two properly exposed rectangles with no stitching errors but the gap left between them was coming out to be way more than desired.

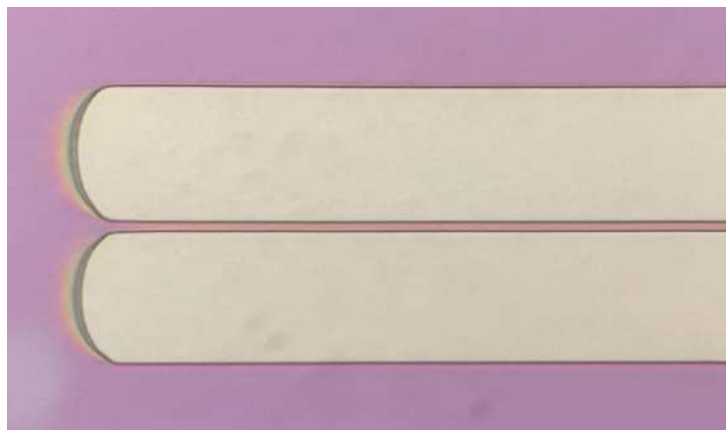


Figure 4.4: Round edges and thick central strip

- Changing the aperture, and hence the beam current, did not change the writing time and also did not change the width of the central strip, which is very unexpected. The left and right edges of the rectangles were curved, because that's how fbms works, and changing the beam current only changed the curvature of that.
- Changing the dose had no effect on anything.
- Changing the width in the design file had very small effect.
- Only changing the calculation width(CW)¹ had a significant effect on the writing time and the width of the central strip. I found that increasing the CW increased the width of the central strip and the same trend with decreasing. But decreasing the calculation width beyond 0.3 microns gave no central strip. So, I found that 0.3 microns CW gave the best results. Also making the rectangles vertical instead of horizontal in the design file gave better results, in terms of thickness of the central strip.
- But still the results were far from satisfactory. First of all, the left and right edges came out to be very curved. Then we didn't have precise control over the width of the central strip as it only depended on the CW and very slightly on the design file. Changing the aperture and dose, practically had no effect. None of this makes any sense with how EBL and FBMS works.
- Then I made a discovery and had a eureka moment, everything now started making sense after this. I discovered a software bug and also found a way to go around it.
- When enabling the FBMS area option the software shows the stage speed for FBMS below that. But I noticed that the speed was always 0.2 mm/s and never any other value. Even when calculating the speed, from the calculator, to be of some other value, the value written below the FBMS area option stayed at 0.2 mm/s. After exploring a little I found another option, in the calculating beam current section, where we can calculate the stage speed and the beam speed and calculating the stage speed from there did update the stage speed below the FBMS area option. And after doing this the writing time changed significantly with aperture/beam current and did not change with changing the calculation width.
- But still the central strip width was way more than desired. Changing the aperture did decrease it significantly but it also increased the writing time significantly. And the left and right edges still came out to be curved, with curvature again decreasing with decreasing aperture.

¹FBMS also asks for another parameter called the calculation width and it is the average width of the FBMS element that we are exposing, it entirely depends on the design file.

- I thought that maybe the machine is trying to create a circle of diameter 20 microns at once and is failing in doing so. So, to prevent this from happening I divided the 20 microns into 10 lines of 2 micron width. And this worked, it gave me a central strip with almost the desired width and the left and right edges were straight instead of being curved.
- There were thin lines of resist in between two lines that was left after developing. To remove this, I introduced 100 nm of overlapping between two consecutive lines.
- To draw tapered design I first drew the tapered edges with fbms and then filled the insides of it using normal area mode.



Figure 4.5: The pad with tapered edges connecting to the central strip

January

- I could draw the entire design in 1.5 hours but there were still two flaws. There were extra resist lines that was left in the meander, this meant that there were still unexposed regions even after overlapping. And the second one was that, the transition from the wide region into the central strip was not smooth, it was thinner and curved/shifted.

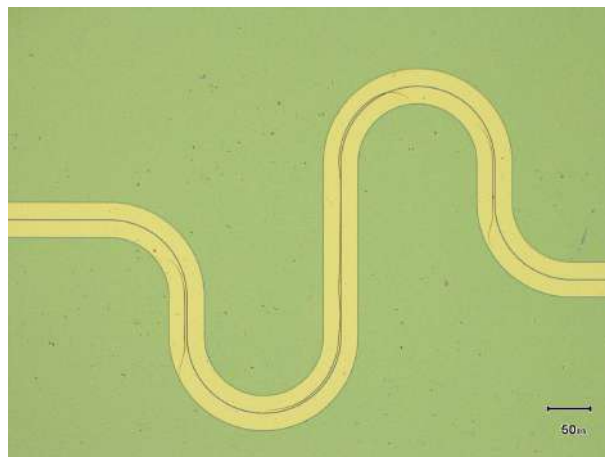


Figure 4.6: Resist residue

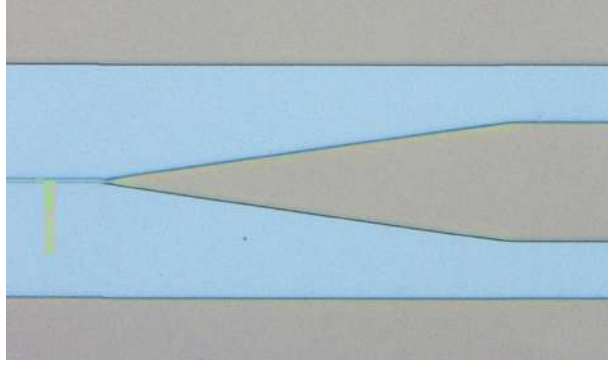


Figure 4.7: Kink at the junction

- Increasing the overlap did seem to get rid of the extra resist from the meander.

February

- There were traces of resist left at several places even after increasing the overlap to various degrees. The solution that I found was to increase the dose from 250 to 275 and not increasing the overlap. This problem was entirely solved after this and I never saw it again.
- The transition from wider region into the central strip was made continuous and smooth by changing the design file such that transition became a single FBMS path and not broken into two separate components.
- Another problem that I faced was that the central strip sometimes broke at one or more than one places after development. This issue was solved by decreasing the development time from 20 seconds to 10 seconds. It still crops up sometimes but very rarely.

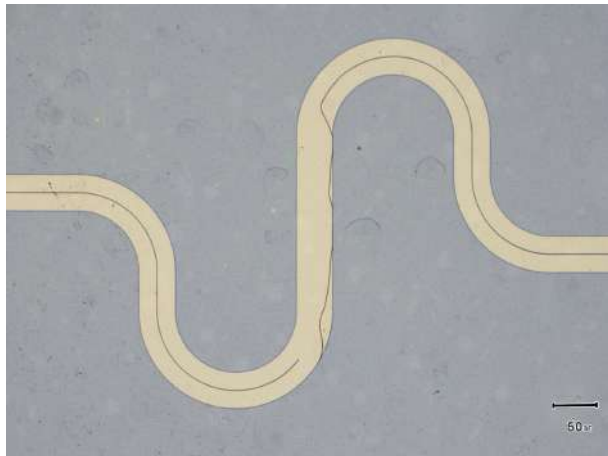


Figure 4.8: Broken central strip

Now the EBL recipe for resonator has been completely optimized for the resist PMMA 950K A6 with a thickness of 500 nm.

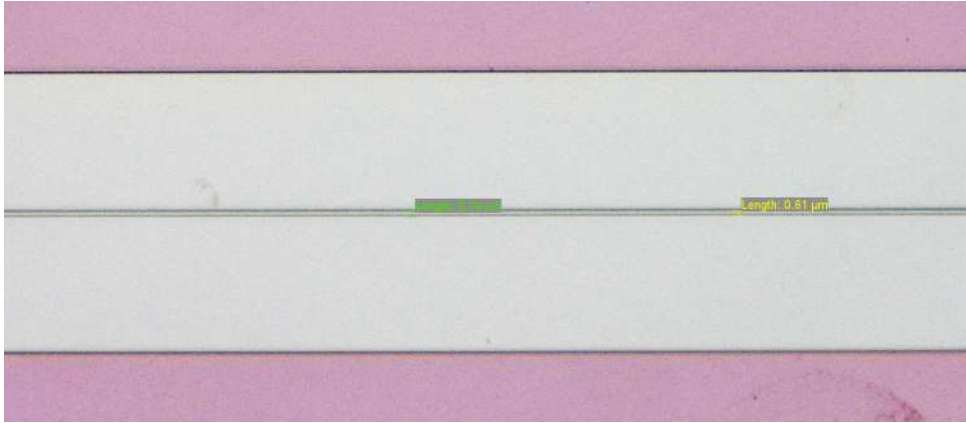


Figure 4.9: Central strip

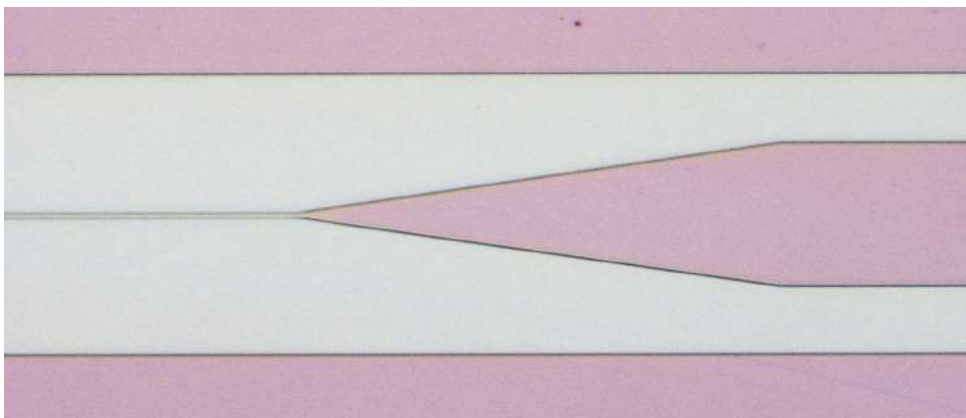


Figure 4.10: Junction

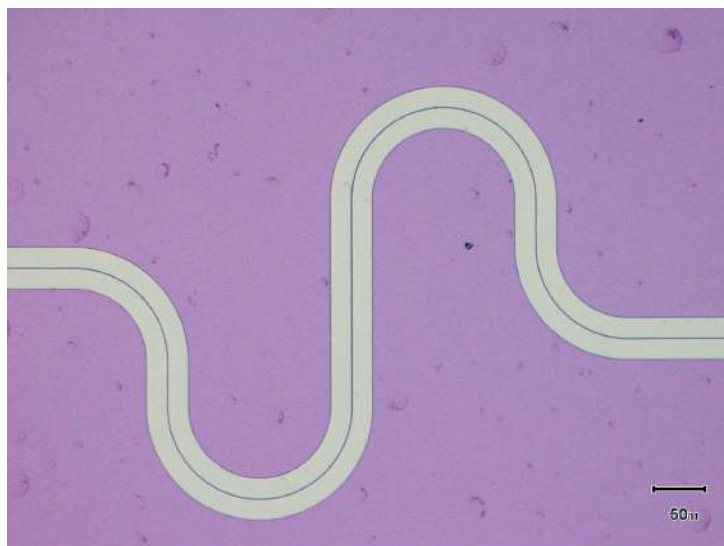


Figure 4.11: Meander

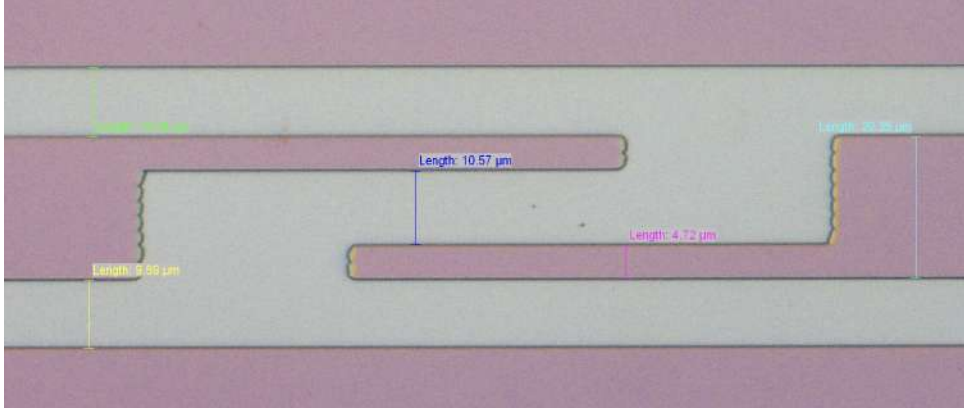


Figure 4.12: Coupling Capacitor

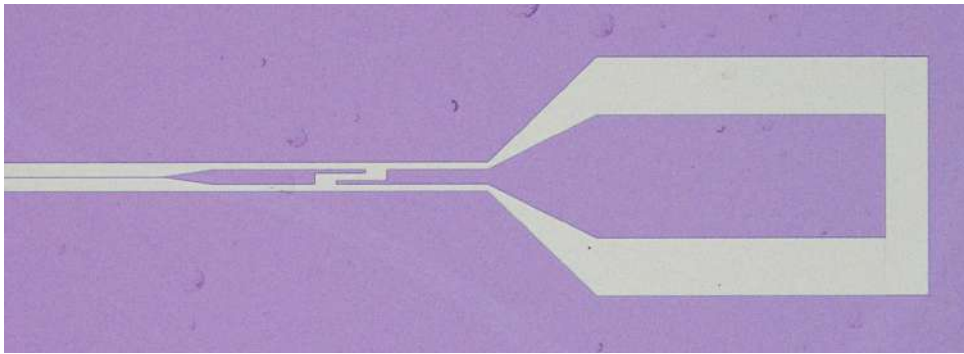


Figure 4.13: Pad

4.3 Design file/GDS file

- The design file has been made in accordance with the requirements of writing using FBMS mode in Raith150Two system as this is the file that the tool uses to expose the exact pattern.



Figure 4.14: Resonator design

- The whole design of $20\text{ }\mu\text{m}$ width has been divided into 10 rectangles of $2\text{ }\mu\text{m}$ width and an overlap of 200 nm . A gap of 600 nm has been left in the middle that will become the resonator after etching.

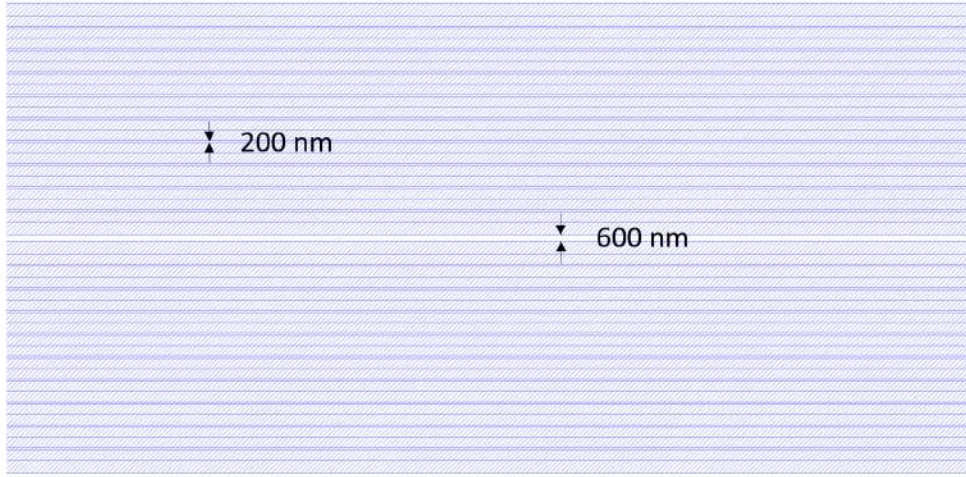


Figure 4.15: FBMS paths with 200 nm of overlap and and gap of 600 nm left in the middle

- The transition from the wider region into the resonator is done using a single FBMS path to maintain the smoothness of the transition.

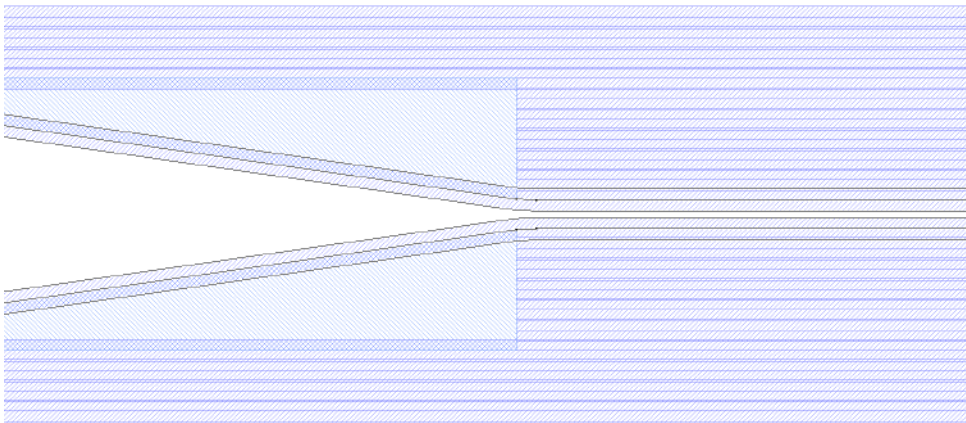


Figure 4.16: Transition from wider region into the resonator

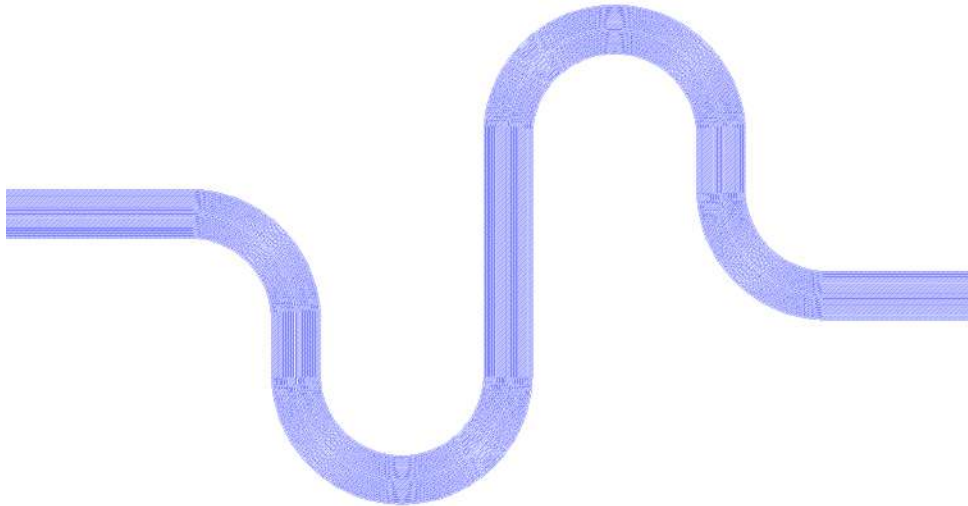


Figure 4.17: Meander

- The capacitor is made from FBMS elements too.

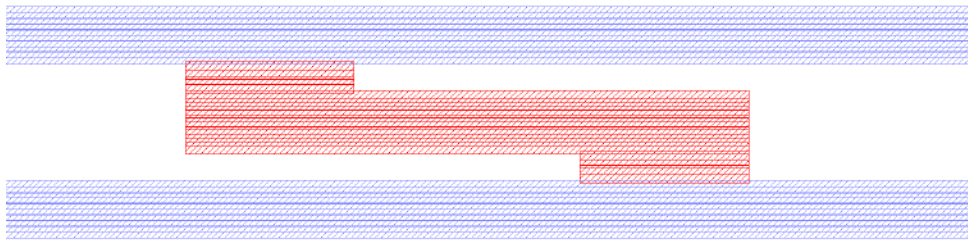


Figure 4.18: Capacitor

- The pads are made from FBMS elements as well. The tapered regions are made by using FBMS mode for their edges and then filling the region inside by using normal mode.

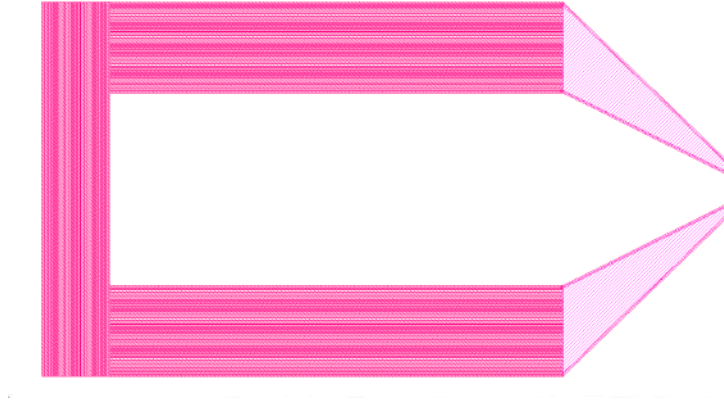


Figure 4.19: Pad

4.4 Etching and Sputtering

- The gas used for NbN etching is CF_4 .



- The first issue was of finding out the correct power at which the NbN etches. After doing several processes I found out that etching at 200 W for 3 minutes gives the resonator on the thin film.
- But there were two issues that arose. First the edge of the central strip was very rough which will affect the resonant frequency and the quality factor of the resonator. Second one was that the NbN film had not etched properly at several places and in worst cases even created a short circuit between the central strip and the ground planes.

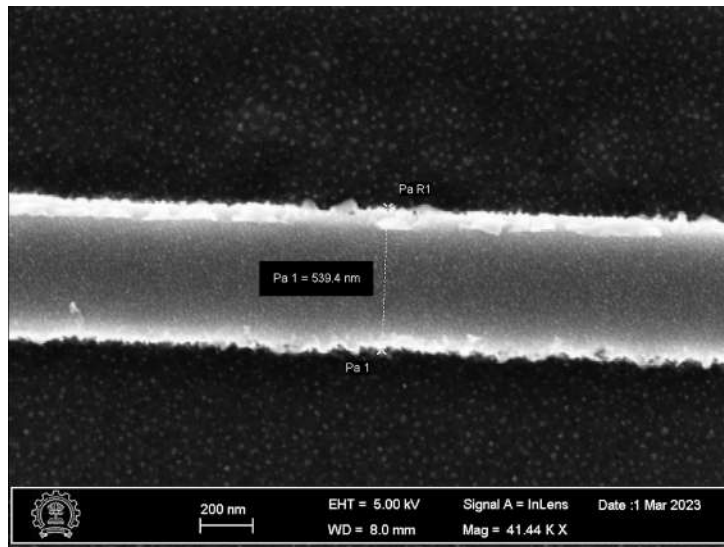


Figure 4.20: Rough edges

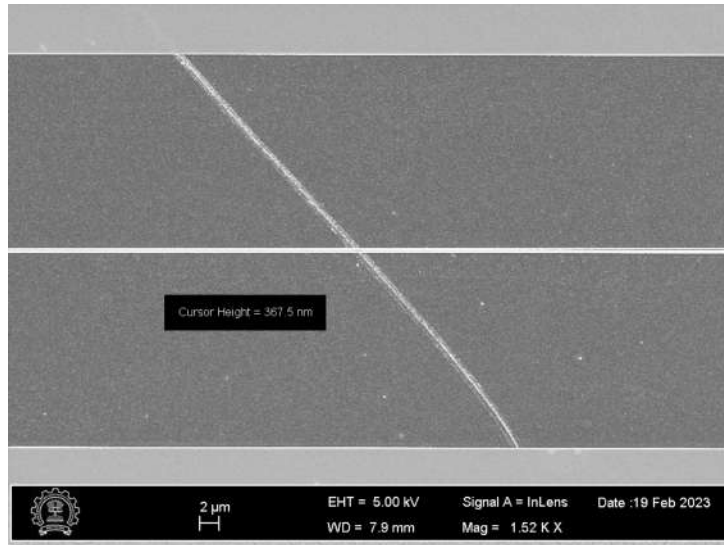


Figure 4.21: Unetched NbN creating a short

- The first issue was resolved by decreasing the power to 150 W and increasing the time to 5 minutes.
- The second issue hasn't been resolved yet. Changing the power or the gas flow rate did not improve the etching at all.
- I tried using other gases like CHF_3 and SF_6 but to no avail.
- Adding oxygen helps but it also increases the rate at which resist etches which then causes other issues.

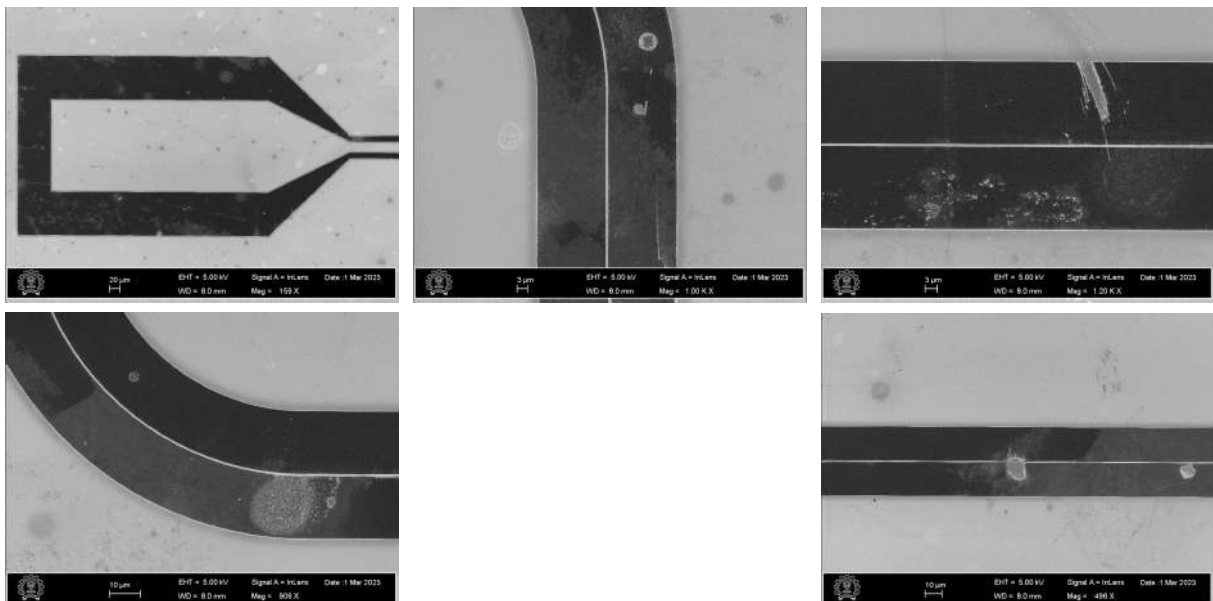


Figure 4.22: Some images of the issues that we were facing with NbN etching

- This issue could be either due to bad film quality or with etching tool STSRIE. To isolate the issue we created a resonator on bare silicon without any NbN on it,

and etching that gave perfect results. The etching was very uniform without any residues. This proved that the issue was with the NbN film deposition.

- In order to remove this issue arising from sputtering I decided to try depositing NbN at 75 W of power instead of 150 W. Doing this solved the issue and the film etched perfectly without any residues.
- I also noticed that etching for 5 minutes also removed most of the resist which then causes the NbN thin film to etch. So to prevent this I decreased the etching time to 4 minutes and it gave the same results as earlier without etching the resist completely.

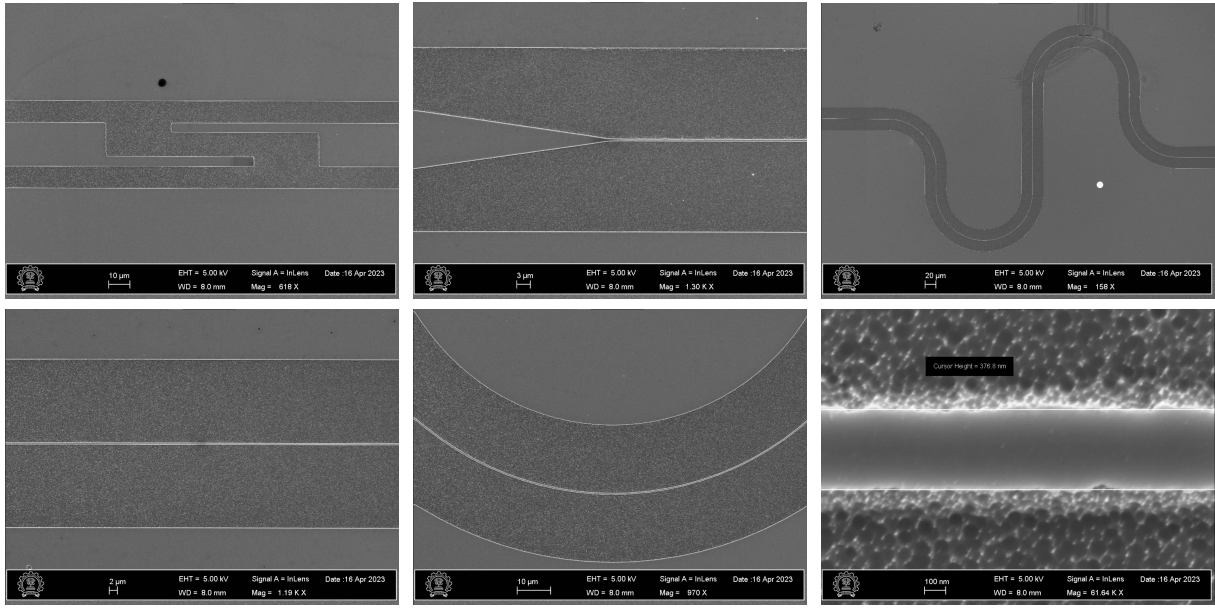


Figure 4.23: Perfect etching but the films were deposited after doing clean biasing

4.5 Final recipes

Sputtering

- Using Sputter Orion
- Target - Nb
- Power - 75 Watts DC
- Chamber pressure - 3 mTorr
- Argon:Nitrogen - 10sccm:8sccm
- Height of the substrate - 40 mm
- Time - 20 minutes

EBL

- Using Raith150Two
- Resist - PMMA 950K A6 spun at RPM: 4000 and Acceleration: 2000 for 59 seconds and baked at 180 °C for 2 minutes.
- Aperture - 30 μm
- Write field - 65.53 μm at 1530x magnification (Not needed for FBMS mode).
- Unselect all modes and select only the FBMS area mode, it'll write both the normal area and FBMS area together in one run.
- Calculation width - 0.2 μm (Only needed for FBMS mode)
- Dose - 300 $\mu\text{C}/\text{cm}^2$ for normal area and 275 $\mu\text{C}/\text{cm}^2$ for FBMS area
- First write the resonator part, then the capacitors and then the pads.
- Develop in MIBK:IPA for 10 seconds and then dip in IPA for 40 seconds.
- Dry the IPA very carefully using very slow flow of nitrogen.

Etching

- Using STSRIE
- Gas - CF_4
- Flow rate - 50 sccm
- RF forward power - 150 Watts
- APC valve - 70
- Gas stabilisation time - 1 minute
- Process duration - 4 minutes

Note: The rate of deposition and the rate of etching hasn't been optimised yet. But the given recipe gives us a resonator with a thin film thickness less than 50 nm.

Chapter 5

Results

5.1 Simulation

The resonator is simulated using Ansys HFSS. HFSS uses a numerical technique called the Finite Element Method(FEM) to simulate electromagnetic fields.

The design for the resonator was made using QCAD and Klayout, saved as a GDS file and then imported into HFSS. It has a dielectric made of silicon of thickness $500\mu m$.

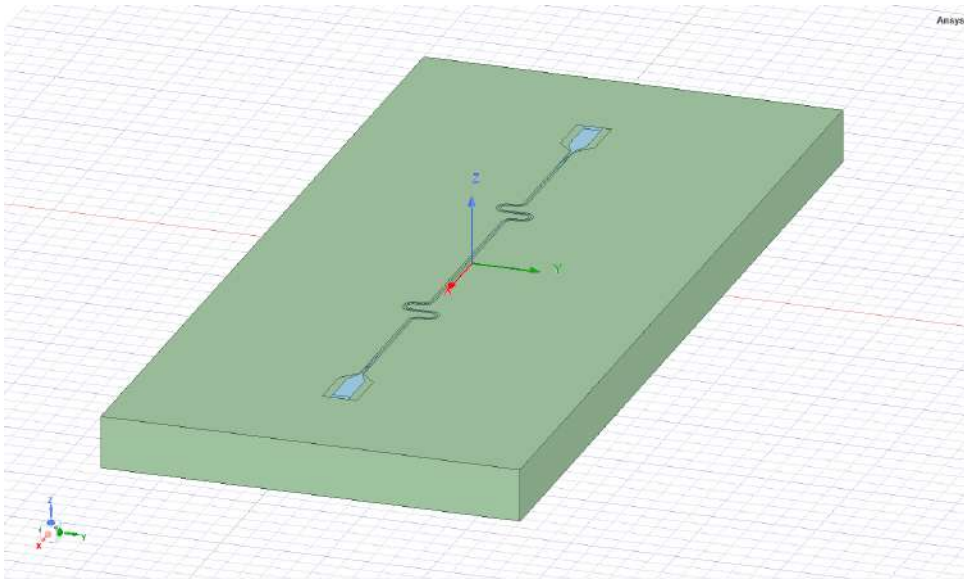


Figure 5.1: Resonator simulated on HFSS

On the top surface, there is a ground plane and the resonator is formed in between the ground plane. The central strip is of width 600 nm and the gap on both sides of the central strip is $20\mu m$.

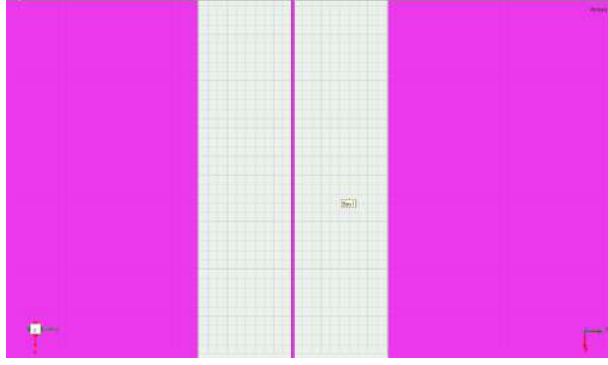


Figure 5.2: Resonator central strip and the gap

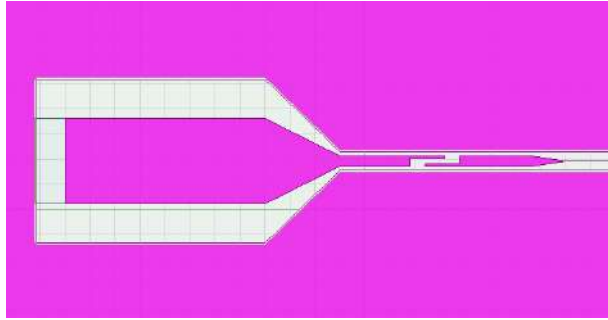


Figure 5.3: Pad and coupling capacitor

Both the resonator and the ground plane have been modeled as 2D surfaces with perfect electrical conductivity.



Figure 5.4: Perfectly conducting ground plane and resonator

The excitation has been modeled as lumped port with an input impedance of $50 \, \Omega$. Both the ports are set up such that the voltage at the ports of the resonator is set up with respect to the ground plane, which is how the ground plane should work. This is done by choosing an integration line from the ground plane to resonator port for both the ports.

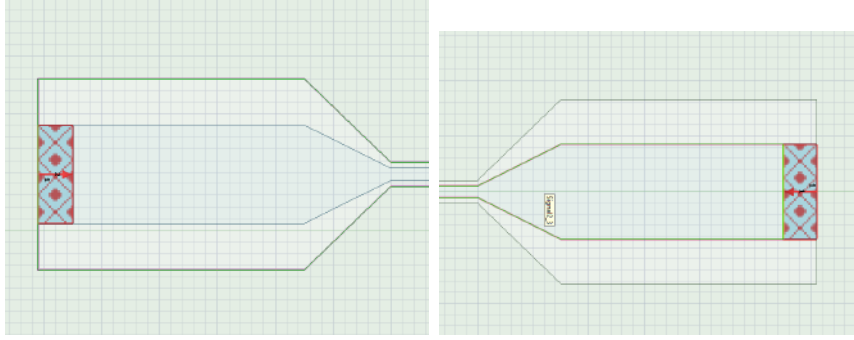


Figure 5.5: Lumped ports

The whole resonator is placed inside a box, this box is called the boundary. HFSS needs to know the details of the boundary inside which it can simulate the design, this boundary defines the simulation space/computational volume. By default, the boundary is set to conducting and this causes the electromagnetic waves that leak out from the resonator to reflect from the boundary and then cause interference with signals inside the resonator. So we override this by creating our own boundaries. We do that by placing the entire design inside of huge box and setting its faces as radiation boundaries, which means that it will absorb all of the radiation that falls onto it and does not reflect anything. The material inside the box is chosen as air.

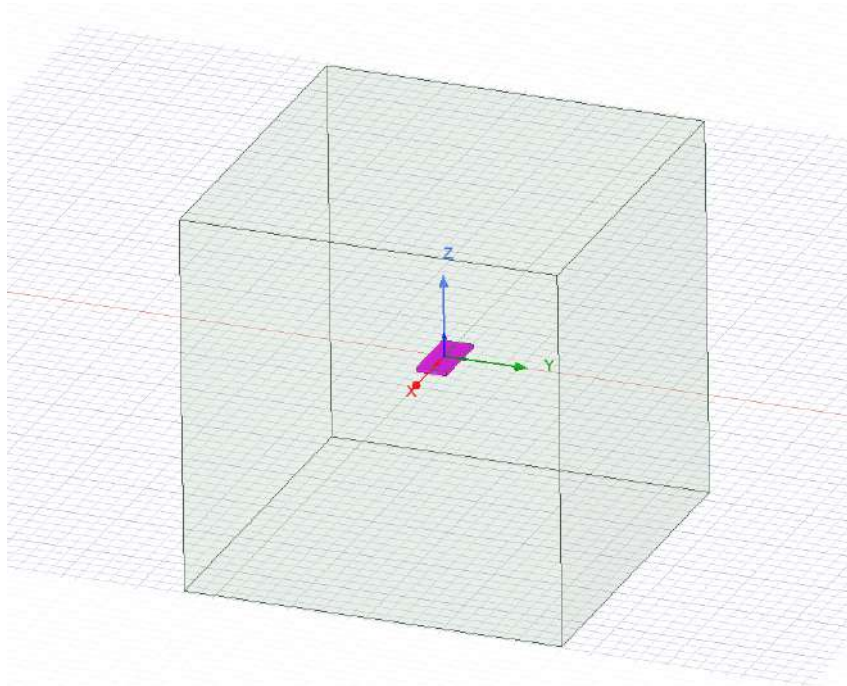


Figure 5.6: Radiation boundary around the resonator

HFSS uses mesh to solve for electric fields at a particular region. It keeps on increasing the resolution the mesh at a particular region until the value of the electric field at that region saturates to a value for successive mesh's with higher resolution. The criteria for convergence and maximum number of passes is something that we can control but in our

case I used the default values.

In the solution setup, I chose the broadband mode in which the mesh is tested for convergence for a range of frequencies. This is used when we don't know the resonant frequency of resonator. There are other options in which the we can solve the mesh only for selected value(s) of frequency.

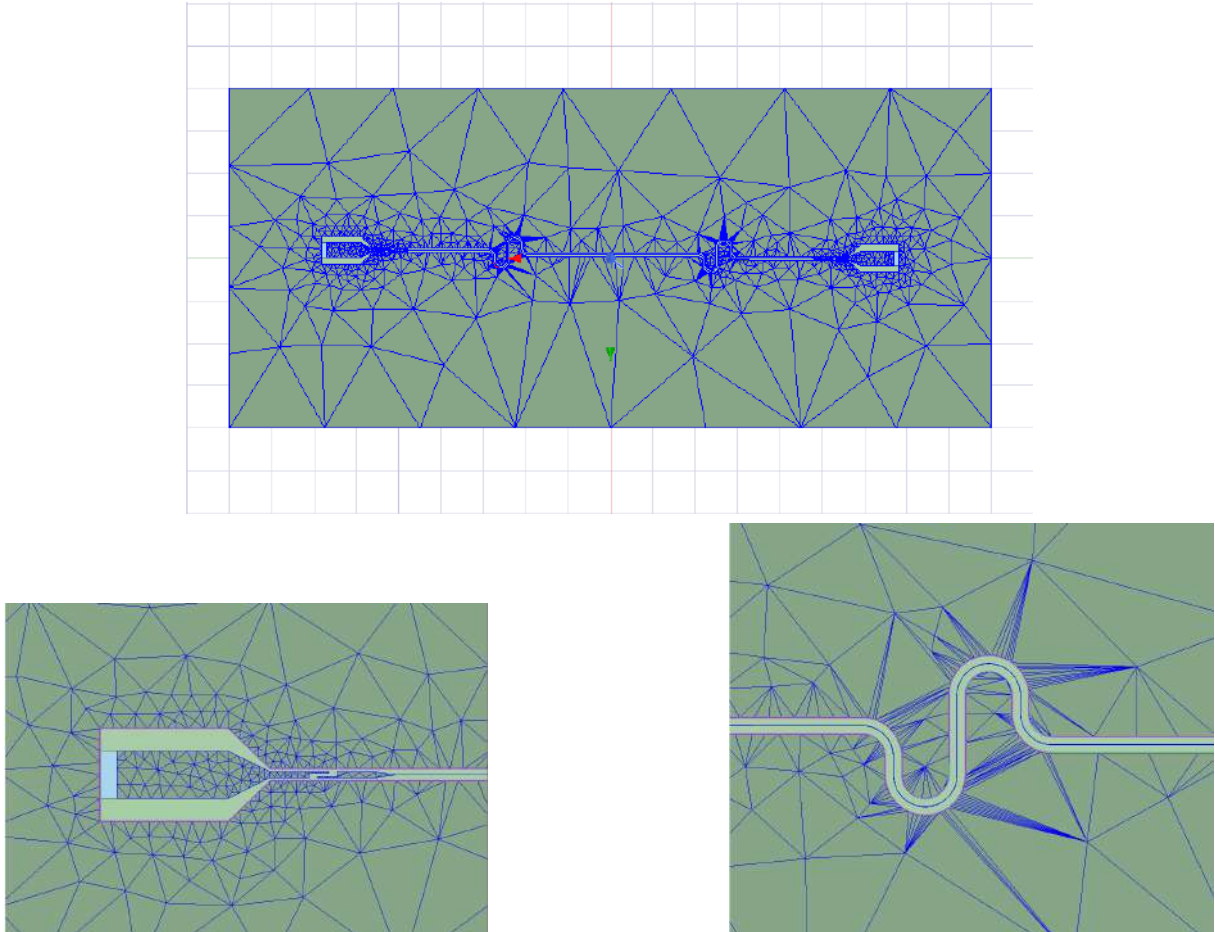


Figure 5.7: Resultant mesh after convergence

For this simulation I solved the mesh in the region 7 GHz to 8 GHz and then performed a sweep in discrete mode from 7 GHz to 8 GHz at 200 points.

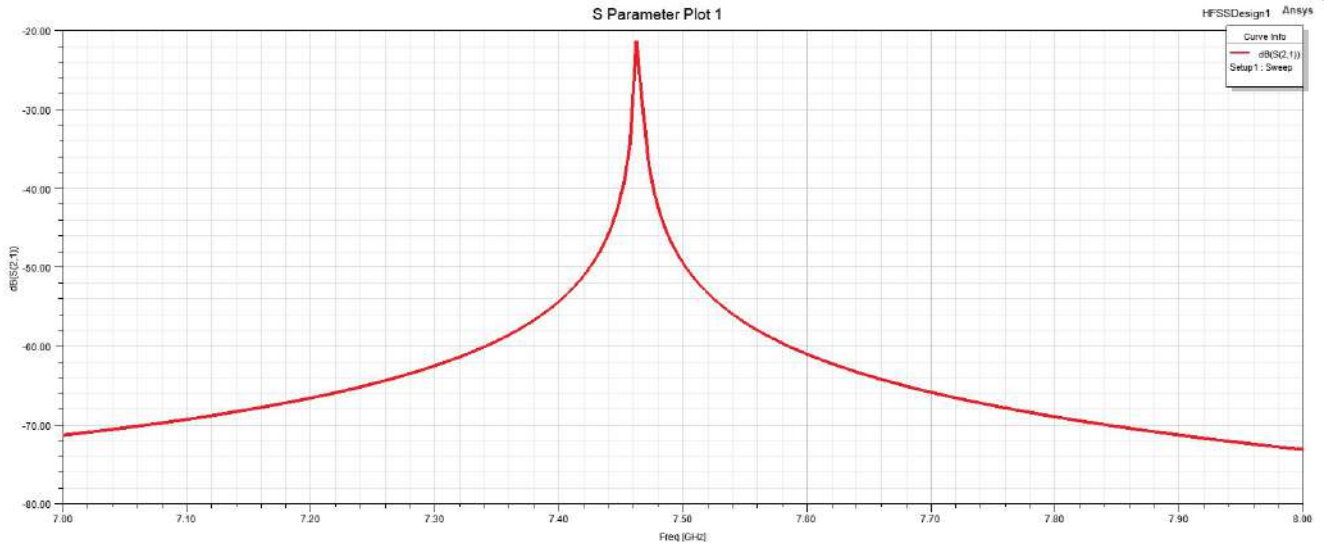


Figure 5.8: S21 parameter

Zooming in we can see that the resonant frequency is 7.46 GHz.

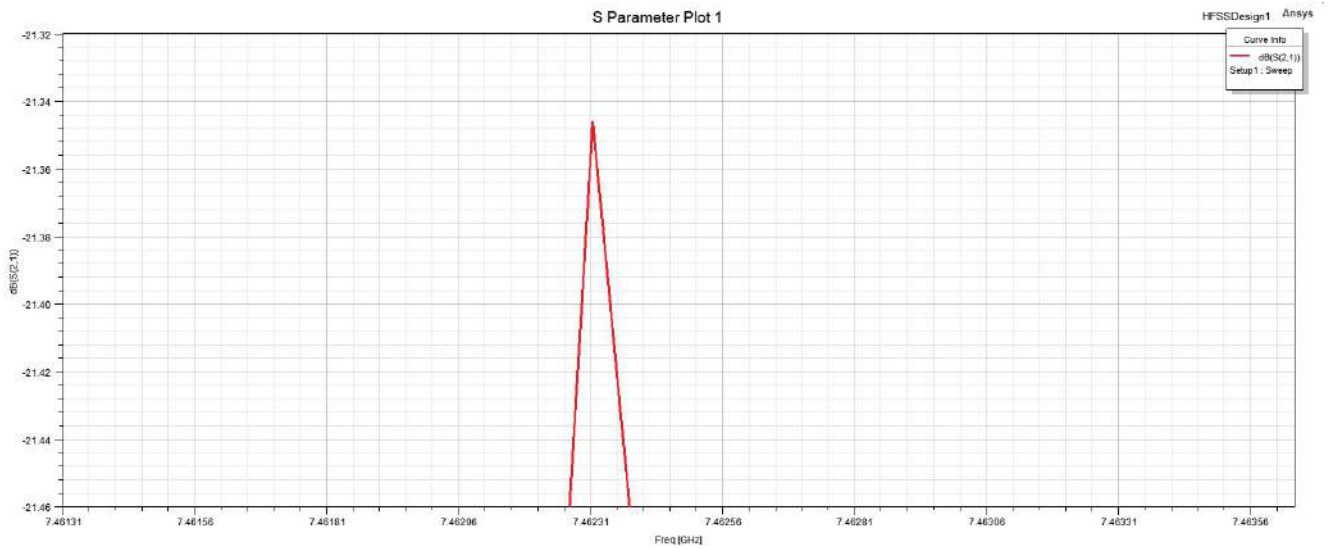


Figure 5.9: Resonant frequency

5.2 Sputtering

By making use of sputtering I am trying to develop a recipe to create NbN thin films with high kinetic inductance and high enough T_c so that it remains a superconductor even in the presence of magnetic fields. We want our film to have these properties because we are going to use these films to make our resonators and as we saw earlier increasing the kinetic inductance will help in coupling the spin qubits to the resonator, which requires superconductivity. Superconductivity also makes resonators low loss, which increases their Q factor.

I have grown 5 different samples of NbN thin films using DC Sputtering with different growth conditions.

1. The first sample was made at 50 W of power for 15 mins. The Ar to N gas flow rate ratio was 10sccm:8sccm. The chamber pressure was maintained at 3 mTorr. The T_c for this sample was measured to be 3.47 K
2. The second sample was made at 150 W of power for 10 mins. The Ar to N gas flow rate ratio was 10sccm:8sccm. The chamber pressure was maintained at 10 mTorr. This sample was not conducting at room temperature, so its T_c wasn't measured.
3. The third sample was made at 150 W of power for 10 mins. The Ar to N gas flow rate ratio was 10sccm:6sccm. The chamber pressure was maintained at 3 mTorr. The T_c was measured to be 12 K.

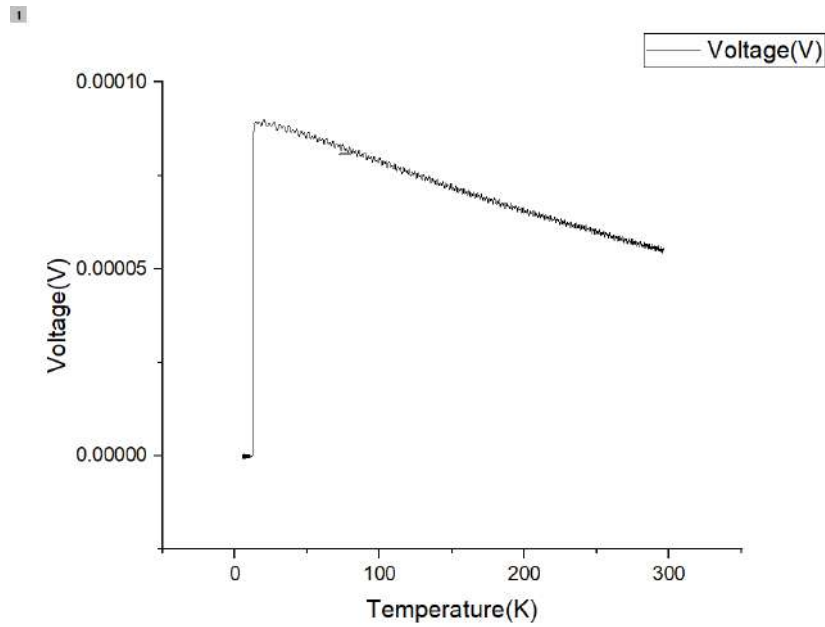


Figure 5.10: Ar:N=10:6 at 3mTorr, $T_c = 12\text{K}$

4. The fourth sample was made at 150 W of power for 10 mins. The Ar to N gas flow rate ratio was 10sccm:8sccm. The chamber pressure was maintained at 3 mTorr. The T_c was measured to be 12.2 K.

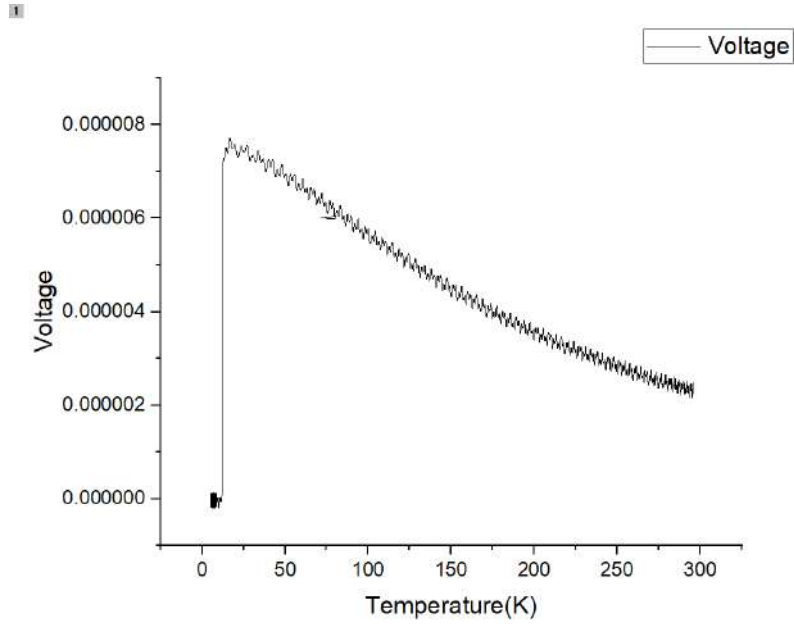


Figure 5.11: Ar:N=10:8 at 3mTorr, $T_c = 12.2\text{K}$

5. The fifth sample was made at 150 W of power for 10 mins. The Ar to N gas flow rate ratio was 10sccm:10sccm. The chamber pressure was maintained at 3 mTorr. The sample did not become superconducting even at 10 mK.

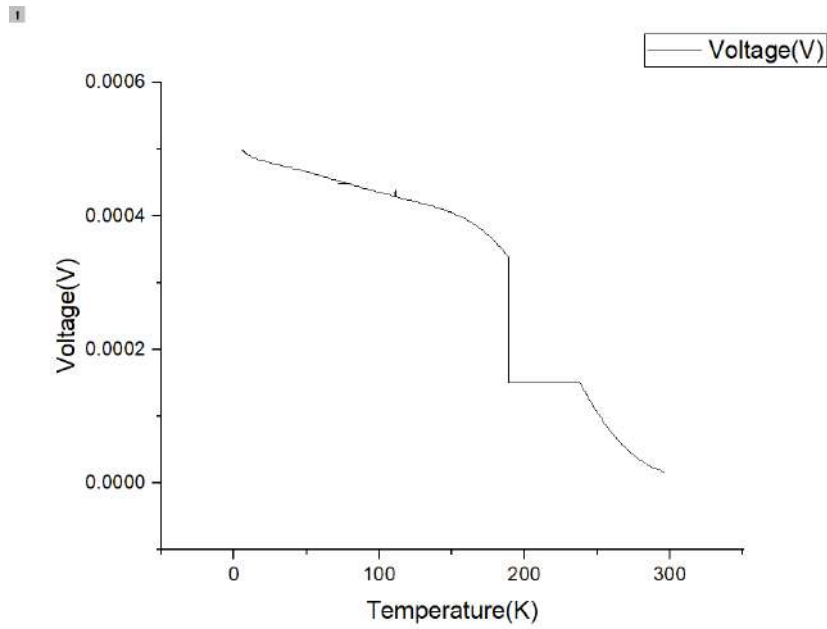


Figure 5.12: Ar:N=10:10 at 3mTorr

5.3 Fabrication

After completion of all the fabrication steps mentioned in the previous chapter we get the following sample.

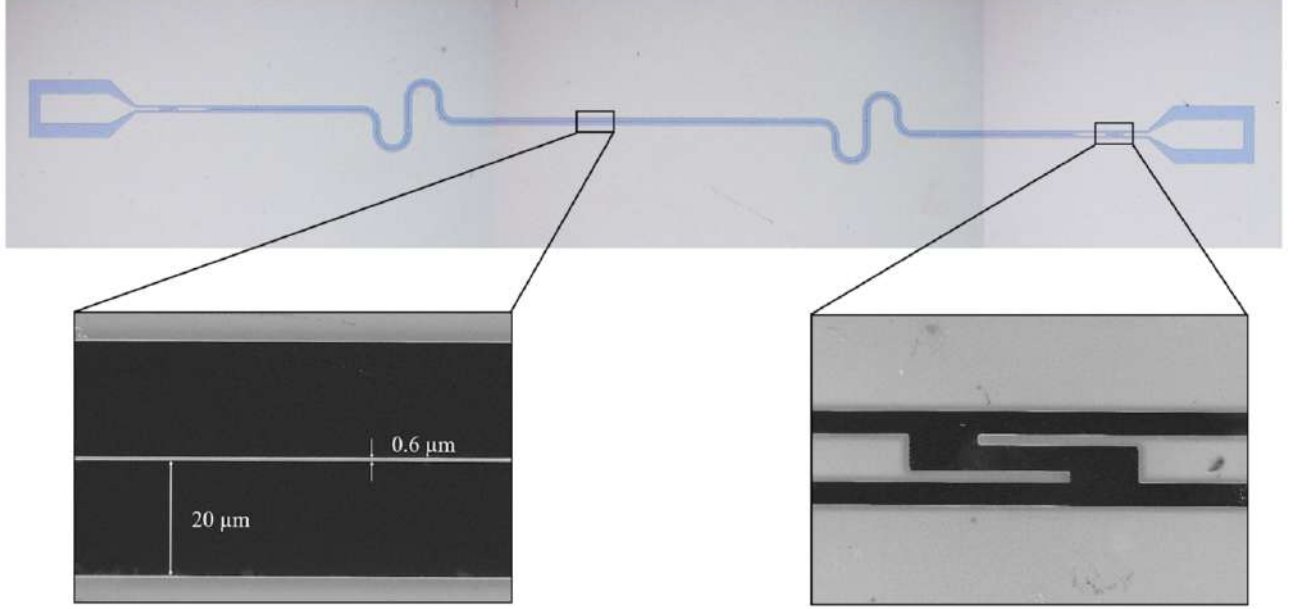


Figure 5.13: Final result after all the fabrication

5.4 Resonator measurement

S21 measurements were performed on the final resonator after all the fabrication steps and we obtained the following results.

From the Phase vs Frequency plot we observe that the frequency at 0 phase is 6.40402 GHz, at 45 phase is 6.32663 GHz and at -45 phase is 6.46207 GHz. Therefore the resonant frequency is 6.40402 GHz, which is less than that obtained by simulation and the reason for that is because simulation does not take into account kinetic inductance. Kinetic inductance will increase the total inductance which will decrease the resonant frequency. The difference between the frequencies at 45 phase and -45 phase gives the FWHM of the S21 plot and is equal to 135.44 MHz. Hence the Q factor is 47.2831.

1

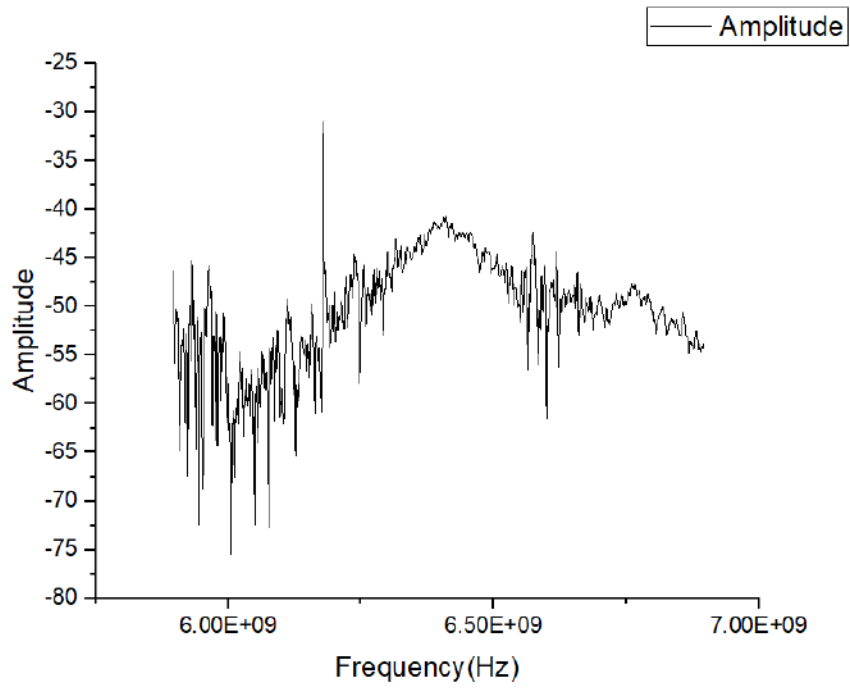


Figure 5.14: Transmission amplitude vs Frequency or S21

1

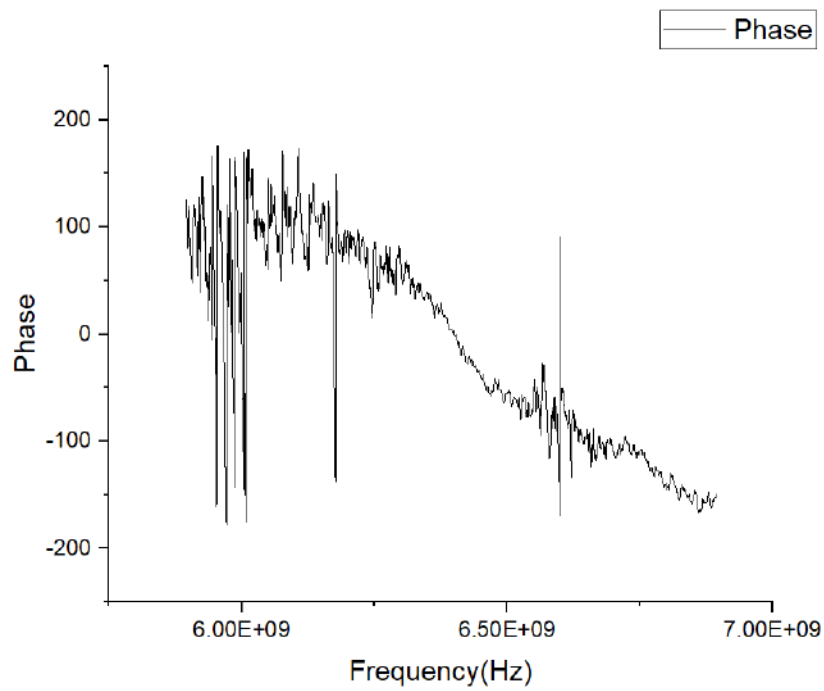


Figure 5.15: Phase vs Frequency

Future Work

Thin films

1. To keep looking for recipes that increase the T_c and kinetic inductance of NbN and NbTiN.
2. To find out the rate of deposition.

Simulation

1. To find out how to calculate Q factor from the simulation.
2. Optimise the design to get high Q factor.

Etching

1. To find out the rate of etching.

Measurement

1. To try and optimise fabrication so that we get high Q factor.
2. We need to check the effect of magnetic field on the resonant frequency and the Q factor.
3. Try using other materials with higher kinetic inductance to see if we can improve on these parameters significantly or not.
4. Then try to couple the resonator to a spin qubit.

Bibliography

- [1] C. Xinqing Yu, S. Zihlmann, G. Troncso Fernández-Bada, J.-L. Thomassin, F. Gustavo, É. Dumur, and R. Maurand, “Magnetic field resilient high kinetic inductance superconducting niobium nitride coplanar waveguide resonators,” *arXiv e-prints*, pp. arXiv-2012, 2020.
- [2] X. Mi, J. Cady, D. Zajac, P. Deelman, and J. R. Petta, “Strong coupling of a single electron in silicon to a microwave photon,” *Science*, vol. 355, no. 6321, pp. 156–158, 2017.
- [3] N. Samkharadze, G. Zheng, N. Kalhor, D. Brousse, A. Sammak, U. Mendes, A. Blais, G. Scappucci, and L. Vandersypen, “Strong spin-photon coupling in silicon,” *Science*, vol. 359, no. 6380, pp. 1123–1127, 2018.
- [4] D. Loss and D. P. DiVincenzo, “Quantum computation with quantum dots,” *Phys. Rev. A*, vol. 57, pp. 120–126, Jan 1998. [Online]. Available: <https://link.aps.org/doi/10.1103/PhysRevA.57.120>
- [5] J. R. Petta, A. C. Johnson, J. M. Taylor, E. A. Laird, A. Yacoby, M. D. Lukin, C. M. Marcus, M. P. Hanson, and A. C. Gossard, “Coherent manipulation of coupled electron spins in semiconductor quantum dots,” *Science*, vol. 309, no. 5744, pp. 2180–2184, 2005. [Online]. Available: <https://www.science.org/doi/abs/10.1126/science.1116955>
- [6] L. V. C. Assali, H. M. Petrilli, R. B. Capaz, B. Koiller, X. Hu, and S. Das Sarma, “Hyperfine interactions in silicon quantum dots,” *Phys. Rev. B*, vol. 83, p. 165301, Apr 2011. [Online]. Available: <https://link.aps.org/doi/10.1103/PhysRevB.83.165301>
- [7] D. Zajac, T. Hazard, X. Mi, K. Wang, and J. R. Petta, “A reconfigurable gate architecture for si/sige quantum dots,” *Applied Physics Letters*, vol. 106, no. 22, p. 223507, 2015.
- [8] R. Hanson, L. P. Kouwenhoven, J. R. Petta, S. Tarucha, and L. M. K. Vandersypen, “Spins in few-electron quantum dots,” *Rev. Mod. Phys.*, vol. 79, pp. 1217–1265, Oct 2007. [Online]. Available: <https://link.aps.org/doi/10.1103/RevModPhys.79.1217>

- [9] X. Xue, T. F. Watson, J. Helsen, D. R. Ward, D. E. Savage, M. G. Lagally, S. N. Coppersmith, M. A. Eriksson, S. Wehner, and L. M. K. Vandersypen, “Benchmarking gate fidelities in a Si/SiGe two-qubit device,” *Phys. Rev. X*, vol. 9, p. 021011, Apr 2019. [Online]. Available: <https://link.aps.org/doi/10.1103/PhysRevX.9.021011>
- [10] J. Majer, J. Chow, J. Gambetta, J. Koch, B. Johnson, J. Schreier, L. Frunzio, D. Schuster, A. A. Houck, A. Wallraff *et al.*, “Coupling superconducting qubits via a cavity bus,” *Nature*, vol. 449, no. 7161, pp. 443–447, 2007.
- [11] E. Jaynes and F. Cummings, “Comparison of quantum and semiclassical radiation theories with application to the beam maser,” *Proceedings of the IEEE*, vol. 51, no. 1, pp. 89–109, 1963.
- [12] A. Blais, R.-S. Huang, A. Wallraff, S. M. Girvin, and R. J. Schoelkopf, “Cavity quantum electrodynamics for superconducting electrical circuits: An architecture for quantum computation,” *Phys. Rev. A*, vol. 69, p. 062320, Jun 2004. [Online]. Available: <https://link.aps.org/doi/10.1103/PhysRevA.69.062320>
- [13] D. Pozar, *Microwave Engineering*, ser. Addison-Wesley series in electrical and computer engineering. Addison-Wesley, 1990. [Online]. Available: <https://books.google.co.in/books?id=0XLFQgAACAAJ>
- [14] K. Watanabe, K. Yoshida, and T. A. Kohjiro, “Kinetic inductance of superconducting coplanar waveguides,” *Japanese journal of applied physics*, vol. 33, no. 10R, p. 5708, 1994.
- [15] Wikipedia contributors, “Sputtering — Wikipedia, the free encyclopedia,” 2022, [Online; accessed 11-November-2022]. [Online]. Available: <https://en.wikipedia.org/w/index.php?title=Sputtering&oldid=1072193347>
- [16] B. Hafner, “Scanning electron microscopy primer,” *Characterization Facility, University of Minnesota-Twin Cities*, pp. 1–29, 2007.